Development of nanoparticle catalysts and total internal reflection (TIR) Raman spectroscopy for improved understanding of heterogeneous catalysis

BINGHAM, LAURA,MARIA

Chapter 4. Development of a synthesis procedure for copper/oleylamine/oleic acid nanoparticles (copper/OAm/OAc nps)

Copper nanoparticles with appropriate capping agents have enormous potential for use as monometallic (or bimetallic) model catalysts to understand and improve the design of catalysts for a variety of transformations. Specifically considered in my work are applications in the heterogeneous catalysis of furfural hydrogenation and ethylene epoxidation two important catalytic processes for which more environmentally benign catalysts are urgently sought (see Chapter 1, Sections 1.6.2, and 1.6.1 respectively). Chapter 6 gives details of new insights based upon the use of copper nanoparticle catalysts supported on γ-alumina for use in furfural hydrogenation as a replacement for undesirable copper chromite materials.

4.1. Results and discussion - monometallic copper nanoparticles

Based on the available literature a number of key factors have been considered and studied systematically from a standardised preparation. The standard synthesis was optimised through careful consideration of each preparation condition. Firstly copper(II) acetylacetonate was chosen as the metal precursor. It is our aim to synthesise silver/copper bimetallic nanoparticles. For this application, it is desirable to have both metals be delivered from the same metal precursor to allow for addition to the same solution in order to facilitate simultaneous reduction. The ready availability of both copper and silver acetylacetonate species made it a suitable candidate. Oleylamine was chosen as the standard capping agent, due to its wide use in the literature for nanoparticle and quantum dot synthesis more generally and because some indicative results suggested it may be easier to remove than some other capping agents (necessary in generating a free surface for catalysis). The mode of action of oleylamine is attributed to its ability to provide high level steric stabilisation to the as-formed nanoparticles.[1–4] Within this chapter (Chapter 4, Section 4.1.1.2) various other capping agents, such as oleic acid and octadecylamine, were tried but did not appear to stabilise the nanoparticles as efficiently as oleylamine alone. Secondly a high boiling point solvent capable of solvating all the reagents was required. Diphenyl ether was chosen as it fitted these requirements. The use of a separate solvent was preferred because it was found to be easier to purify the nanoparticles subsequently (by washing and precipitation). This is not the case when a large quantity of the oleylamine capping agent itself is used as the solvent, as is often the case in the literature.[5–7] The failure to remove this excess capping

agent is evident in the reduction in the quality of transmission electron microscopy (TEM) images obtained when large amounts of oleylamine are still present, but furthermore may have deleterious effects on their use as catalysts if large quantities of carbon-based material poison the catalyst surface. A standard preparation temperature of 200 °C was selected, although as can be seen in Section 4.1.1.1 various temperatures have been investigated. 200 °C was chosen as it gave reduction of the metal both in the presence and absence of additional reducing agent, and tended to give nanoparticles with limited agglomeration as well as access to particles of a small average size. A reducing agent was not used in all preparations, but when one was used morpholine borane complex was chosen for the standardised conditions. As can be seen from Section 4.1.2 this reducing agent appeared to have given the most efficient and reproducible reduction of the metal precursor. Finally, a standard ripening time of 1 h was employed. This was chosen as investigation of a variety of ripening times (Section 4.1.1.1) indicated that in most cases an equilibrium particle size distribution was reached within 1 h of ripening. The experimental work undertaken, under these standardised conditions, was sub-divided into three sections. A brief description of these three differing experimental conditions is given below.

Monometallic copper nanoparticles by solvent reduction method (no additional reducing agent)

In the absence of additional reducing agent the capping agent (oleylamine) was added to the solvent (diphenyl ether) and the system heated to the desired reaction temperature (200 °C). The metal precursor (copper(II) acetylacetonate) was then added at this temperature, and the reaction was stirred and held at this temperature for 1 h. The reaction solution was cooled to room temperature and washed (Chapter 2, Section 2.2.1.5).

Monometallic copper nanoparticles with additional reducing agent

For synthesis in the presence of additional reducing agent the reducing agent (morpholine borane) was first added to the solvent (diphenyl ether) and stirred at 80 °C for several hours to ensure full dissolution of the reducing agent. Once in solution the reducing agent was added to the capping agent (oleylamine) and the remaining solvent and the solution heated to the specified temperature (200 °C). The metal precursor (copper(II) acetylacetonate) was then added at this temperature, and the reaction was stirred and held at this temperature for 1 h. The reaction solution was cooled to room temperature and washed (Section 2.2.1.5).

Monometallic copper nanoparticles with complexation of the capping agent and metal precursor

The synthesis was further modified to allow complexation of the metal precursor (copper(II) acetylacetonate) and the capping agent (oleylamine). The metal precursor and capping agent were stirred overnight in the solvent (diphenyl ether) at a temperature below that at which reduction of the metal precursor might occur (80 °C). If no additional reducing agent was required then the solution was heated to the specified temperature (200 °C) and ripening for the desired time (1 h) took place. The solution was cooled to room temperature and washed (Section 2.2.1.5). If additional reducing agent was required the solution was heated to a temperature below which reduction will occur in absence of a reducing agent (175 °C) and a solution of fully solvated reducing agent (morpholine borane complex) in the reaction solvent (diphenyl ether) was quickly added. The solution was then ripened at 180 °C for the desired time (1 h) and cooled to room temperature prior to washing (Section 2.2.1.5).

It should be noted that for all TEM data given in the sections that follow particle size for spherical or oval shapes were counted by their typical diameter. Hexagonal shapes were calculated using their long diameter (perhaps resulting in very slightly overestimating their size), but for cubes a mathematical average of their longest (corner to corner) and shortest (side to side) cross particle lengths was used.

4.1.1. Monometallic copper nanoparticles by solvent reduction method (no additional reducing agent)

4.1.1.1. Temperature and time variation

As discussed in the introduction Section 1.5.2 the nucleation and growth stages in nanoparticle synthesis are crucial in determining the properties of the particles obtained. Theories such as classical nucleation theory, Ostwald ripening, and digestive ripening, are key in understanding such behaviour, yet the mechanism operating in any particular case is difficult to elucidate. Temperature during nanoparticle synthesis has a significant impact upon particle nucleation and growth, and upon the outcomes expected when each of the mechanisms above are operational. This might be the enhanced solubility of particles in hotter solutions, or the impact upon kinetics of different stages of reaction.

For nanoparticle synthesis by metal salt reduction, high solution temperatures are often used to facilitate the precursor reduction to the metallic oxidation state. Increased reaction temperatures might be expected to shorten the time taken to reduce the metal salt. This in turn can lead to reductions in the time taken for the particles to nucleate, which may be

desirable in providing “burst” nucleation. Equally, however, the rate of nanoparticle growth will also increase in the hotter solution, as may rates of various ripening processes. The former (nucleation) leads to more particles forming and so smaller particles being expected at higher temperatures, whereas growth processes dominating leads to larger particles being expected from higher preparation temperatures, since growth processes depend on one or both of two thermally activated processes, diffusion transport to the particle surface and a surface reaction. The effect of temperature on the particle size distribution is less clear and depends on whether a particular ripening or coalescence mechanism is dominant.

To investigate this a series of experiments based on the work of Mott *et al.,*[7] but simplifying as many conditions as possible, were conducted investigating the impact of varying reaction temperature, for three varying ripening times (ripening time is the period for which the reacting solution is maintained at temperature). While the choice of solvent, a high boiling point ether, and precursor, copper(II) acetylacetonate, were kept similar or the same, the alcohol reducing agent 1,2-hexadecane diol used by Mott *et al*.,[7] was initially omitted as copper(II) acetylacetonate is also able to decompose thermally to the metal by oxidation of the ligand.[8] The impact of different reducing agents is separately studied below, including 1,2-tetradecanediol, very similar to the 1,2-long-chain-alkanediol that was used by Mott *et al*..[7] The omission of the reducing agent necessitated higher temperatures to cause a reaction to occur. Oleic acid as a capping agent was not used for both simplicity and because oxidation of the product after the reaction was found to be rapid in the presence of oleic acid (although this may not be the case for the situation in which additional reducing agent is present). For convenience, a summary of the key differences between our initial screen and that of Mott *et al.* are given in Table 4.1.[7] A full list of all preparation conditions trialled can be found in the Appendix.

Table 4.1. A summary of key variables comparing the standard preparation in this work to that of Mott et al.,[7] for capping agents oleylamine (OAm), oleic acid (OAc), octadecylamine (ODA).

Parameter	Mott *et al.*	This section
Solvent	Octyl ether.	Diphenyl ether.
Capping agent	OAc, and OAm.	OAm, OAm and OAc and ODA.
Ripening temperature	150 to 210 °C.	200 to 240 °C.
Ripening time	30 min.	10, 30, 60, 120, 180, 240 min.
Reducing agent	1,2-Hexadecanediol.	None unless states.
Procedure	Heated up with all reagents present.	Metal precursor injected at temperature.

Firstly, the impact of ripening time and temperature are explored. These parameters are considered together because although temperature increases the rate of all thermally activated processes, two processes may increase differently (have different activation energies) and so the relative favour of different processes can be changed at different temperatures, but this is only seen/known by monitoring the process as a function of time.

4.1.1.1.1. Temperature variation (1 h ripening time)

From Figure 4.1, an increase in temperature from 200 °C to 220 °C, may have given a very slight increase in overall particle size, but essentially particles were consistently all around 40 nm.

The 230 °C and 240 °C data sets did not follow this trend, a different regime appeared to dominate at higher temperatures.

HREM TEM images show roughly spherical coalesced particles ~ 40 nm formed at 200 °C and 210 °C (Figure 4.2, A-C, Figure 4.3 D), apparently originating from the attachment or coalescence of multiple individual particles. At 220 °C the two batches differ slightly. The first batch (Figure 4.3 E) showed the same coalesced particles as seen for lower preparation temperatures (some appearing hexagonal in profile or less distinctly originating from individual particles). The second batch (Figure 4.3 F) shows a mixture containing some approximately square profile particles. These squarer (or hexagonal) particles exhibit no obvious sign of comprising of multiple individual coalesced particles, and additionally are apparently smaller than the coalesced particles in the same mixture.

Above 220 °C faceted crystallites of distinct shape became more dominant (Figure 4.3 G, Figure 4.4 H, I, J, and K), but also exhibit a much-reduced particle size at 230 °C, which was reproducible. The fact their shapes become better defined indicating greater faceting and the reduced particle size suggest that over the course of the hour, at elevated temperature, the particles have either restructured from those seen at lower temperature or else were formed *via* a different process than was dominant at lower temperature.

At 240 °C again larger particle sizes are again generally obtained (we suspect the smaller size is anomalous, but include this point for completeness). These again (less distinctively) result from the clustering of smaller 'sub-particles'. This was indicative (as had been at 230 °C) of either ripening induced reconstruction or of a different process than was dominant at temperatures below 230 °C.

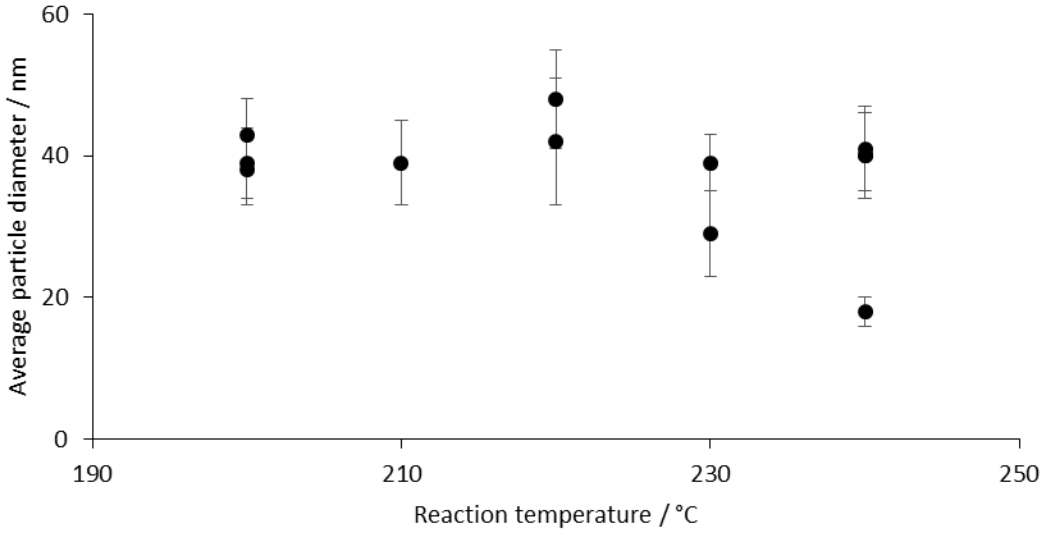

Figure 4.1. Average particle size, and size distributions for particles synthesised according to Section 2.2.1.5 in the absence of reducing agent. TEM images, particle size distributions and sample identifiers are given in Figures 4.2-4.4. Error bars shown represent the standard deviation in particle diameters measured for a minimum of 100 particles.

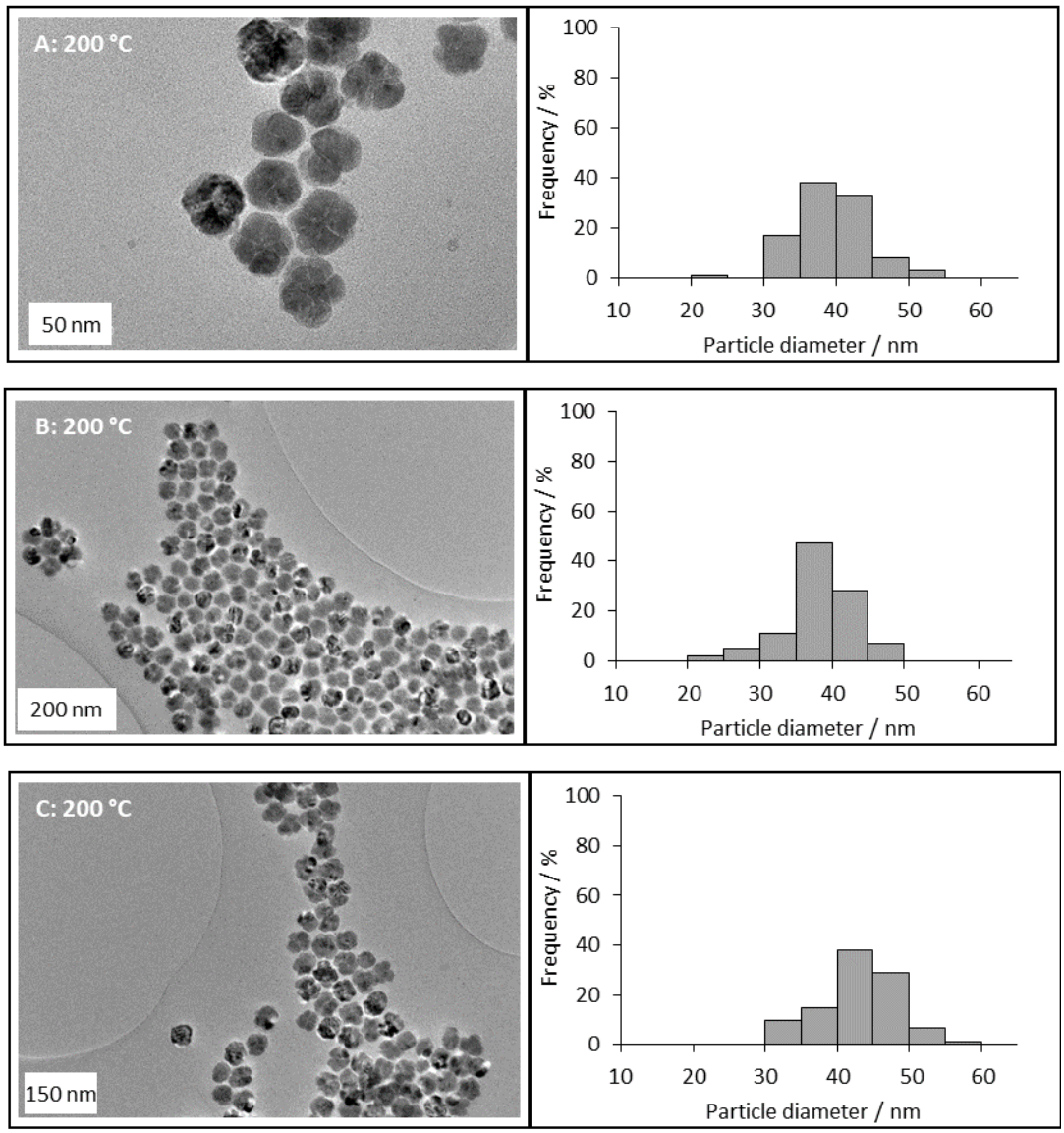

Figure 4.2. TEM images, and histograms calculated from measurement of particle diameter from TEM images for a minimum of 100 particles. For nanoparticles synthesised according to Section 2.2.1.5, in the absence of a reducing agent, with the following ripening temperatures and sample names (see Appendix) A-C) 200 °C, Cu-031215_1, Cu-120716_1 , and Cu-240316_2 respectively.

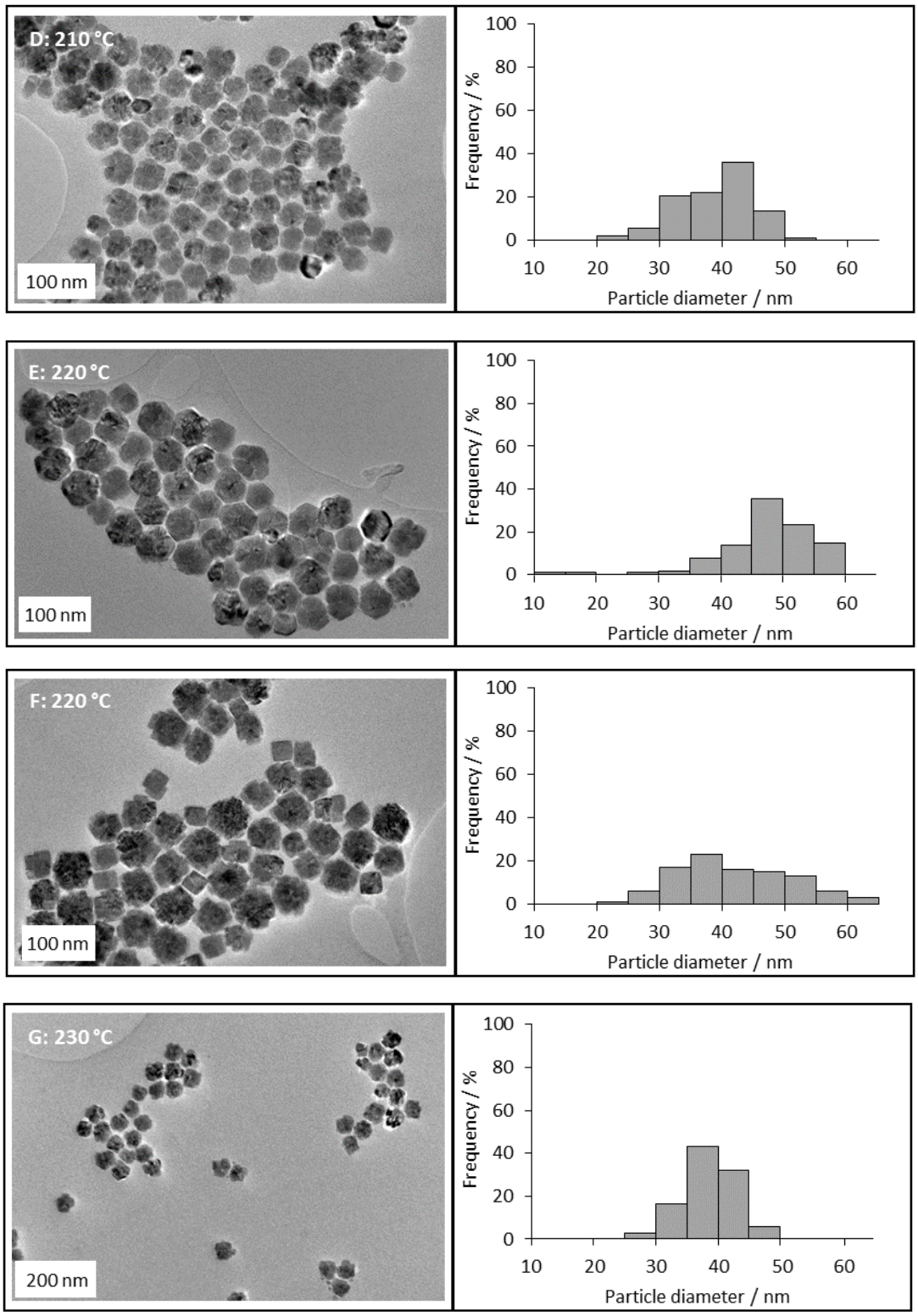

Figure 4.3 TEM images, and histograms calculated from measurement of particle diameter from TEM images for a minimum of 100 particles. For nanoparticles synthesised according to Section 2.2.1.5, in the absence of a reducing agent, with the following ripening temperatures and sample names (see Appendix) D) 210 °C, Cu-180216_1 E-F) 220 °C, Cu-210716_1 and Cu-180216_2 respectively, G) 230 °C, Cu-190216_1 .

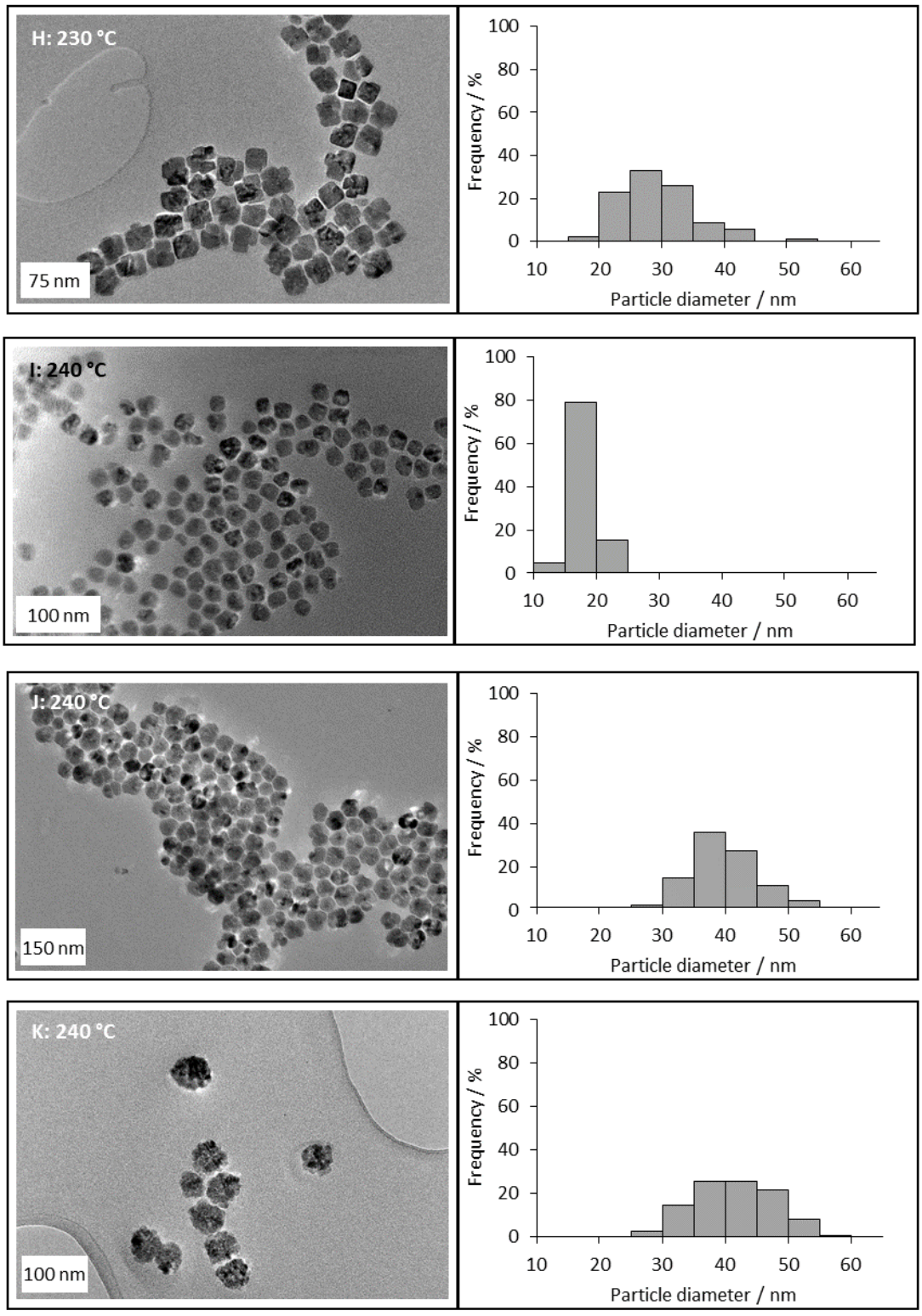

Figure 4.4. TEM images, and histograms calculated from measurement of particle diameter from TEM images for a minimum of 100 particles. For nanoparticles synthesised according to Section 2.2.1.5, in the absence of a reducing agent, with the following ripening temperatures and sample names (see Appendix) H) 230 °C, Cu-080316_1 respectively, I-K) 240 °C, Cu-091215_1, and Cu-020216_1 respectively.

4.1.1.1.2. Temperature variation (10 min, and 30 min ripening times)

For the two extremes of temperature studied above the reaction time was varied. This was undertaken in order to understand whether the temperature was merely speeding up processes that occurred slowly at lower temperatures, or imparting a different outcome on the synthesis. Results from ripening times of 10 min are shown in Figures 4.5, and 4.6. The results appeared to roughly replicate those for the 1 h ripening time, although being slightly smaller in size, and now with particles at both 200 °C and 240 °C appearing to derive from clustering of several smaller particles or breakdown of larger particles. The fact that at both temperatures slightly smaller sizes are obtained than for 1 h ripening times suggested that some growth or ripening occurs between 10 and 60 min. At 30 min (Figure 4.7), similar sizes are again seen, suggesting a gradual growth or ripening occurs. Noticeably, the width of the particle size distributions for an individual batch is seen to increase slightly as a function of time, suggesting digestive ripening (which would result in restructuring to a single preferred size) is not occurring or at least not dominant over other processes. It is therefore likely there is either additional copper in solution still being reduced over the course of the 1 h reaction or Ostwald ripening is occurring. At 30 min the 200 °C samples still appear to derive from the clustering of several smaller particles, whereas the 240 °C particles appear more faceted (as in the 1 h case). It can therefore speculatively be suggested that the coalesced structures at ten minutes have formed from multiple particles, and then at long times and higher temperature significant ripening occurs. Whereas at short times or lower temperatures this process remains incomplete. Continuing the reaction at 240 °C to longer times (2-4 h) resulted in little overall change, although a possible slight gradual reduction in size was seen (Figures 4.8 and 4.9).

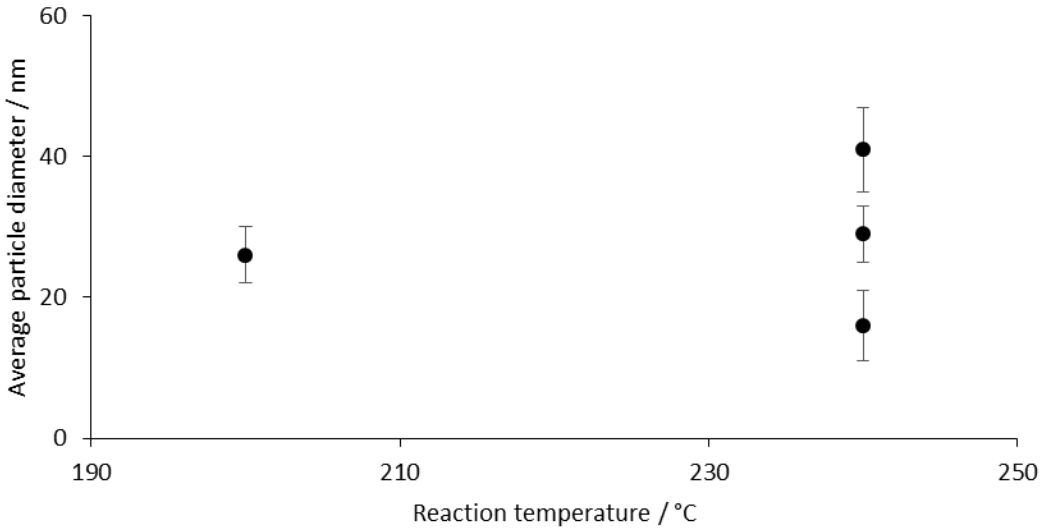

Figure 4.5. Average particle size, and size distribution for particles synthesised according to Section 2.2.1.5 in the absence of reducing agent, and a 10 min ripening period. TEM images, particle size distributions, and sample identifiers are given in Figure 4.6. Error bars shown represent the standard deviation in particle diameter measured for a minimum of 100 particles.

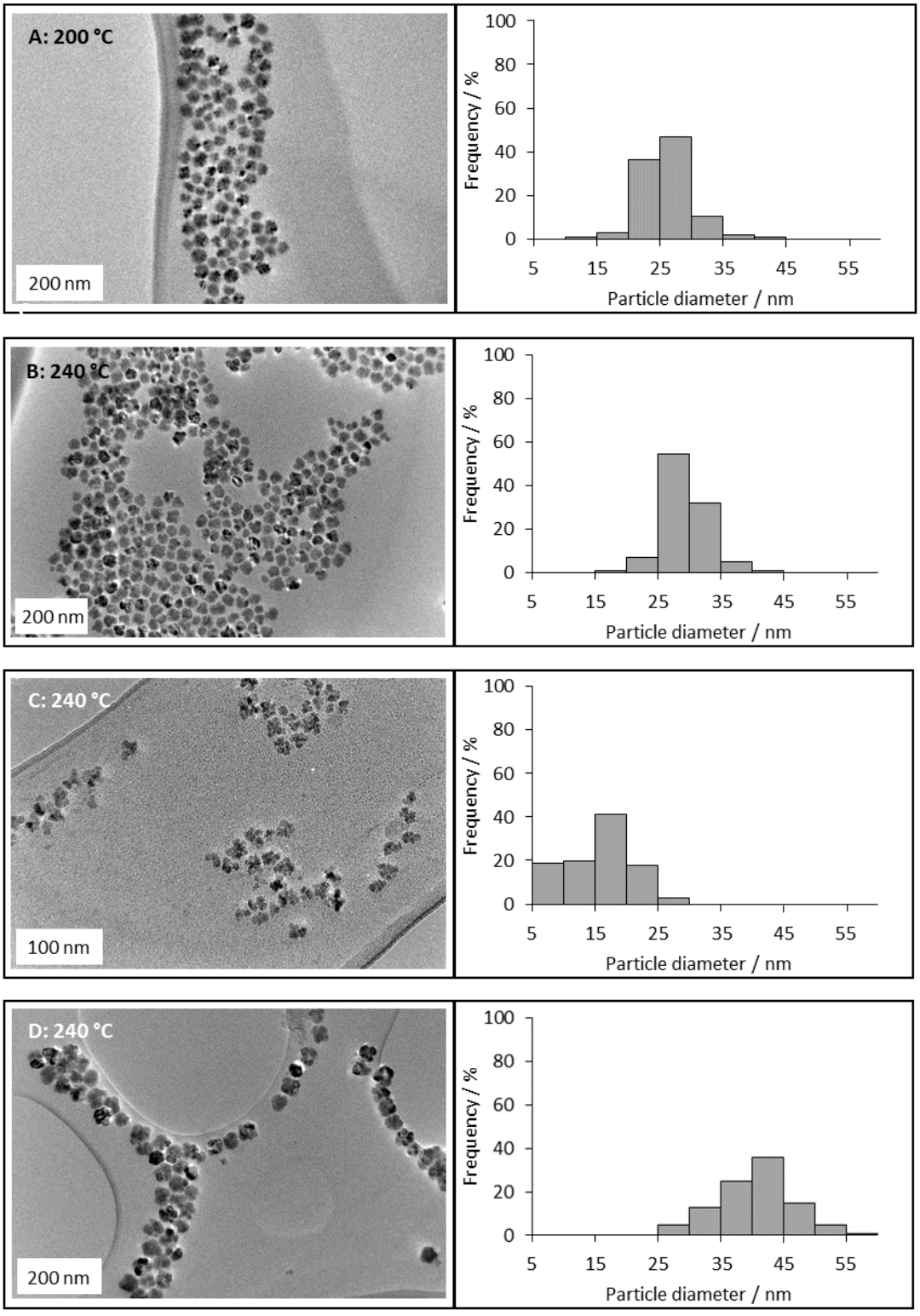

Figure 4.6. TEM images, and histograms calculated from measurement of particle diameter from TEM images for a minimum of 100 particles. For nanoparticles synthesised according to Section 2.2.1.5, in the absence of reducing agent, and a 10 min ripening period with the following ripening temperatures and sample names (see Appendix) A) 200 °C, Cu-161215_1, B-D) 240 °C, Cu-161215_2, , Cu-200116_1, and, Cu-010216_1 respectively.

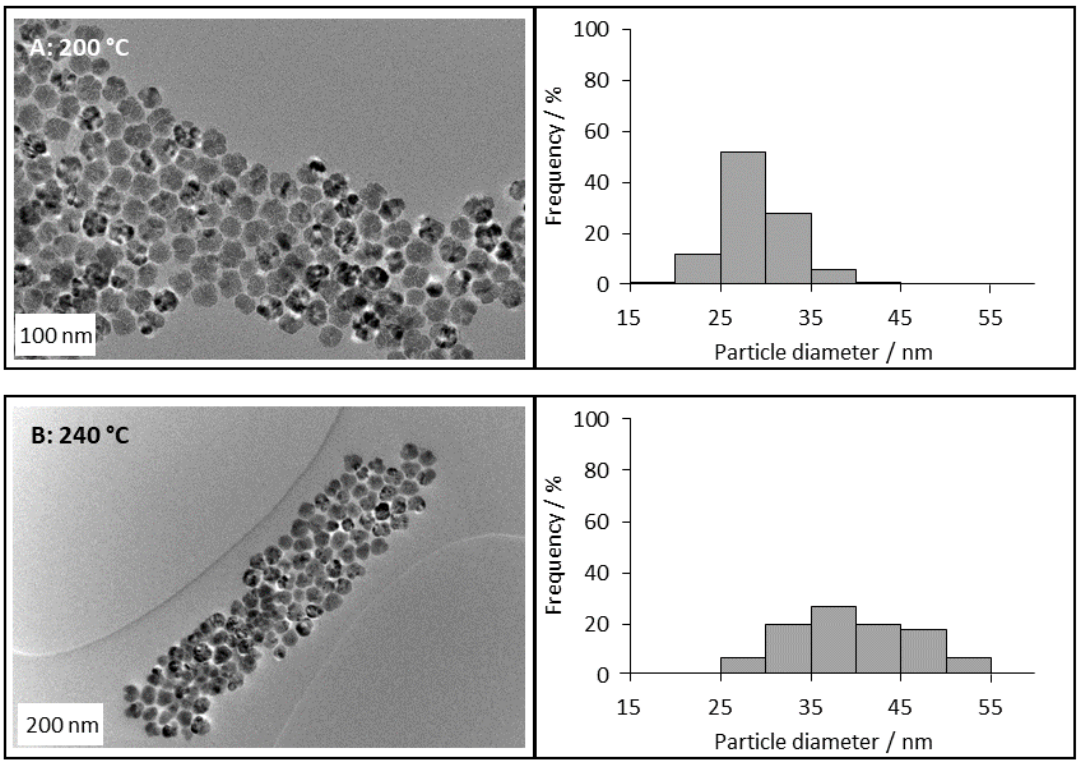

Figure 4.7. TEM images, and histograms calculated from measurement of particle diameter from TEM images for a minimum of 100 particles. For nanoparticles synthesised according to Section 2.2.1.5, in the absence of reducing agent, and with a 30 min ripening period with the following ripening temperatures and sample names (see Appendix) of A) 200 °C, Cu-091215_2, and B) 240 °C, Cu-010216_2. Variation in the reaction temperature resulted in particle size distributions of 29 ± 4 nm, and 40 ± 7 nm for particles shown in images A and B respectively.

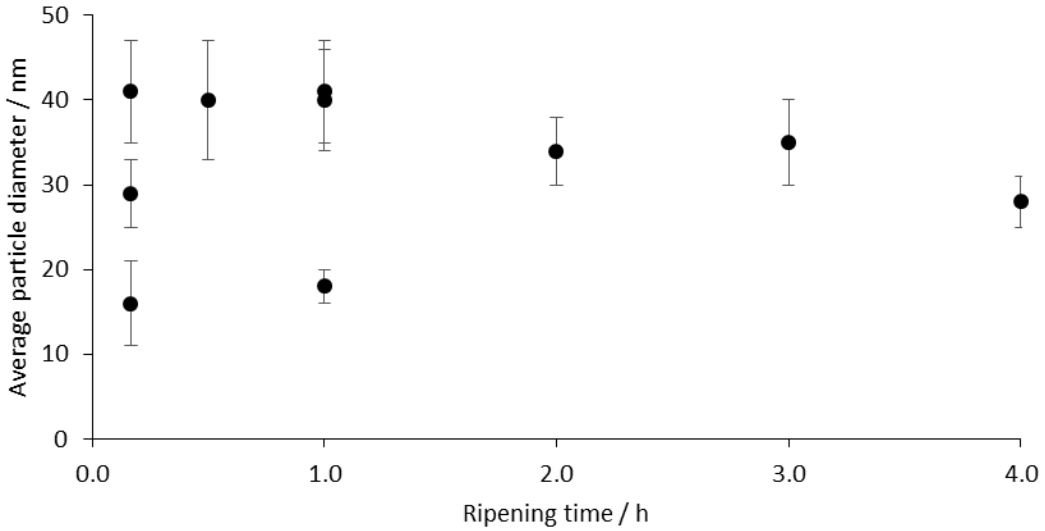

Figure 4.8. Average particle size, and standard deviation for particles synthesised according to Section 2.2.1.5 at 240 °C, for varying ripening times. TEM images, particle size distributions, and sample identifiers are given in Figure 4.9. Error bars shown represent the standard deviation in particle diameter measured for a minimum of 100 particles.

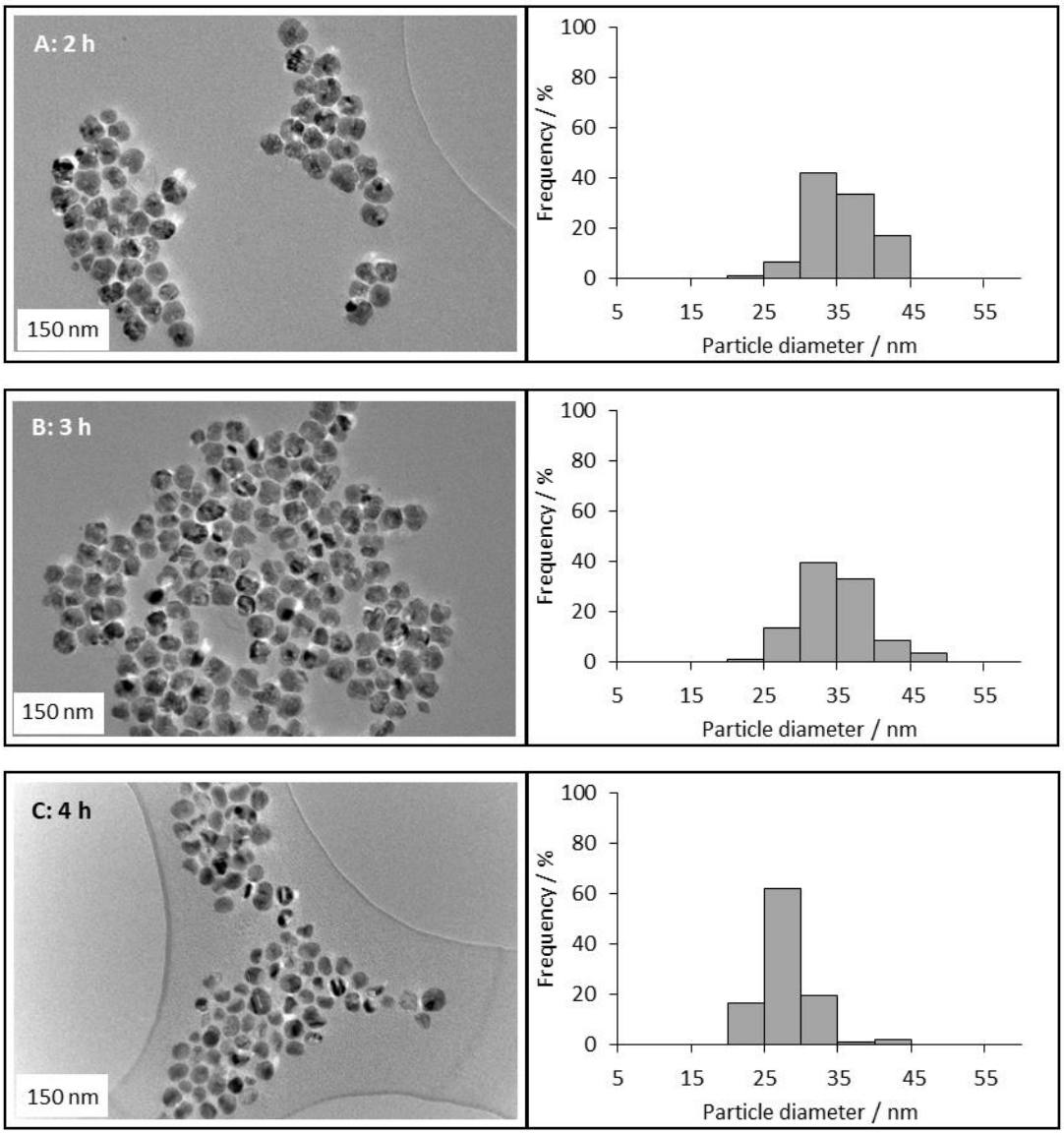

Figure 4.9. TEM images, and histograms calculated from measurement of particle diameter from TEM images for a minimum of 100 particles. For nanoparticles synthesised according to Section 2.2.1.5 at 240 °C with sample names (see Appendix) A) 2 h ripening time Cu_010216_5, B) 3 h ripening time Cu_010216_6, C) 4 h ripening time Cu_010216_7.

4.1.1.1.2.1. Comparison with Mott *et al*. procedure

Having simplified the procedure outlined by Mott *et al*. a number of features are seen in common between the two methods.[7] The authors also reported the loss with increasing temperature of particles that appeared to be formed from coalesced smaller particles, as shape formation and faceting dominated. They believed this was indicative of a switch in reaction mechanism. Further discussion of this work can be found in Section 1.5.3.

Contrary to the observation of Mott *et al.,*[7] rods were not favoured shapes at high temperatures (or indeed formed at all) in this case, and instead square or hexagonal particles dominate. This shows there is no simple relation as to which shapes form most readily, for

copper nanoparticles at high temperatures. It might be that other reagents present contributed to the change in surface energy of certain facets resulting in differences in shape formation. Certainly, the authors believed the nature of the capping agent to be crucial in shape formation (see Section 4.1.1.2 for details) and in the present case oleylamine was the only capping agent used, whereas Mott *et al.* used both oleylamine and oleic acid.[7] They also used a different solvent and reducing agent (octyl ether and 1,2-hexadecanediol respectively) these, or the reducing agents oxidation product could all potentially be responsible for favouring different shapes (present only in their work and not the present case). Seeding mechanisms are dominant in the literature, where the particles grow from seeds (small particles) that have certain facets on their surface obstructed by preferential adsorption of the shape directing species.[9–13] This type of mechanism could be operational here or in the formation of rods in the Mott *et al.* case,[7] although from the fact that the faceted shapes appear after longer times or temperatures, from the initial clustered smaller particles, it seems likely that, at least in the present case, shape formation occurs during ripening rather than growth. In the present case the migration of atoms to maximise low surface energy facets and remove high surface energy ones could alone lead to the types of shapes seen (hexagonal or square in profile), since these mirror those the types of shape obtained for fcc crystal Wulff constructions.[14]

The switch from coalesced clusters of smaller particles to more distinctively shaped particles with clear facets occurs as either time or temperature is increased. This suggests one sequential mechanism is operating in which nucleation, growth and aggregation of small clusters occurs at low temperatures (200-220 °C), or short times (<10 min). Increasing the temperature or time results in Ostwald ripening or slow growth on the 10-60 min timescale, at least for higher temperatures. The generally smaller overall size and narrower distributions at lower times are indicative of Ostwald ripening or slow growth rather than digestive ripening.

Although further experiments could shed more light on this process, the overall sizes of nanoparticles obtained throughout these experiments showed it was not possible to obtain materials of suitable size for catalytic applications (most catalyst metal particles are below 10 nm in order to obtain an acceptable surface area). The focus of the project therefore moved to investigate other variables in the synthesis method.

4.1.1.2. Capping agent investigation

The role of the organic capping agent is to provide steric stabilisation to prevent aggregation of the nanoparticles (Section 1.5.3). Therefore, increasing the amount of capping agent might be expected to provide enhanced stabilisation. It is instructive to consider the amount of capping agent relative to the amount theoretically required to fully cover the nanoparticle surface (Section 2.2.1.5.1). Increasing the quantity of the capping agent could in principle stabilise a higher surface area of metal and so provide access to smaller particle sizes, which have inherently larger surface areas.[15] The nature of the chemical structure of the capping agent is also an important parameter and the subsequent addition of oleic acid or the replacement of oleylamine with the saturated analogue octadecylamine have been investigated.

4.1.1.2.1. Variation of oleylamine capping agent concentration

Table 4.2 shows the effect of doubling the capping agent concentration upon the particle size and size dispersity, for standardized conditions of 200 °C and 1 h ripening time. Although the size dispersity increased with increasing capping agent concentration, the particle size did not vary significantly. TEM images (Figure 4.11) showed a nanoparticle structure based on multiple coalesced particles is the same for both capping agent concentrations. The slightly broader particle size distribution in the presence of more capping agent could be attributed to the presence of impurities in the capping agent, or the capping agent acting as "heterogeneous" nucleation sites or non-standard nucleation sites. Such sites result in nucleation at a separate time to the rest of the sample, and so for this reason it is preferable to minimise excesses of any reagents that play no other role in the synthesis. It should also be noted that using unnecessarily large quantities of oleylamine can cause difficulties in particle purification, and so also in TEM imaging, due to the greasy nature of this organic capping species.

For Figure 4.10 oleylamine concentration was varied comparably to that seen in Table 4.2, but now under conditions that were previously found to produce strongly faceted particles (240 °C and 1 h ripening) rather than particles comprising of multiple smaller spherical components. At this higher temperature a decrease in particle size was seen for the doubled capping agent concentration. Based on the previous assertion that sequential formation of particles comprising multiple smaller particles and then ripening to form faceted particles occurs, it seems the first process is insensitive to capping agent concentration, while in the second step the oleylamine plays a significant role. Speculatively a digestive ripening

mechanism could now be suggested when a large excess of the organic capping agent is used. TEM images for this data set are shown in Figure 4.12 and 4.13 (for entries A-C the 1.1 mol oleylamine concentrations were repeated from Figure 4.2).

Table 4.2. Average particle size, and standard deviation for particles synthesised according to Section 2.2.1.5 with 0.23 mmol copper(II) acetylacetonate at 200 °C with varying amounts of oleylamine (OAm) capping agent. TEM images, particle size distributions, and sample identifiers are given in Figure 4.11. †Note this sample is a repeat included to show reproducibility.

OAm/ mol	particle size / nm	standard deviation / nm	standard deviation / %
1.1	39	5	13
1.1†	38	5	13
2.2	34	5	15

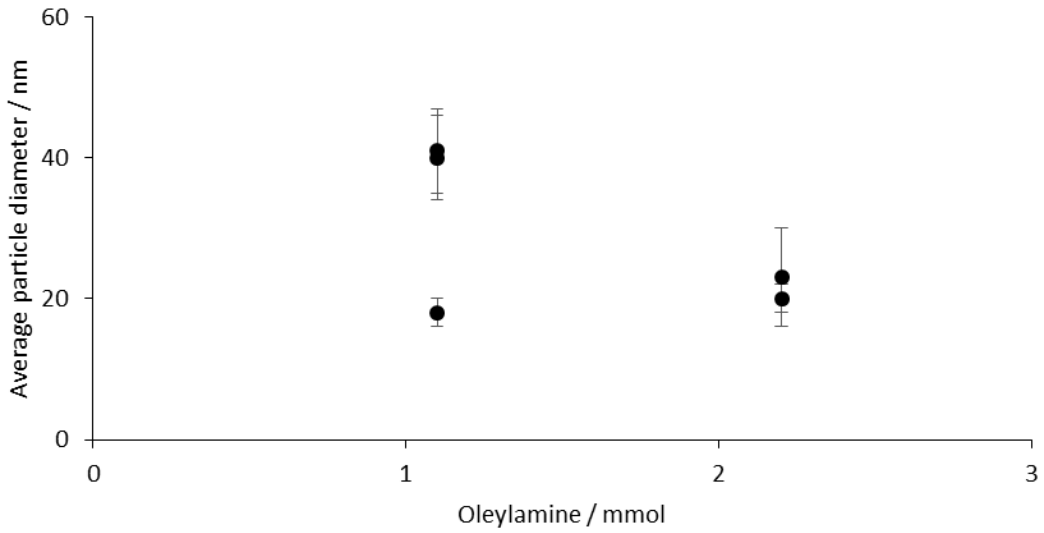

Figure 4.10. Average particle size, and size distribution for particles synthesised according to Section 2.2.1.5 for a 240 °C ripening temperature, with 0.23 mmol copper(II) acetylacetonate, with a varying oleylamine content. TEM images, particle size distributions, and sample identifiers are given in Figures 4.12 and 4.13. Error bars shown represent the standard deviation in particle diameter measured for a minimum of 100 particles.

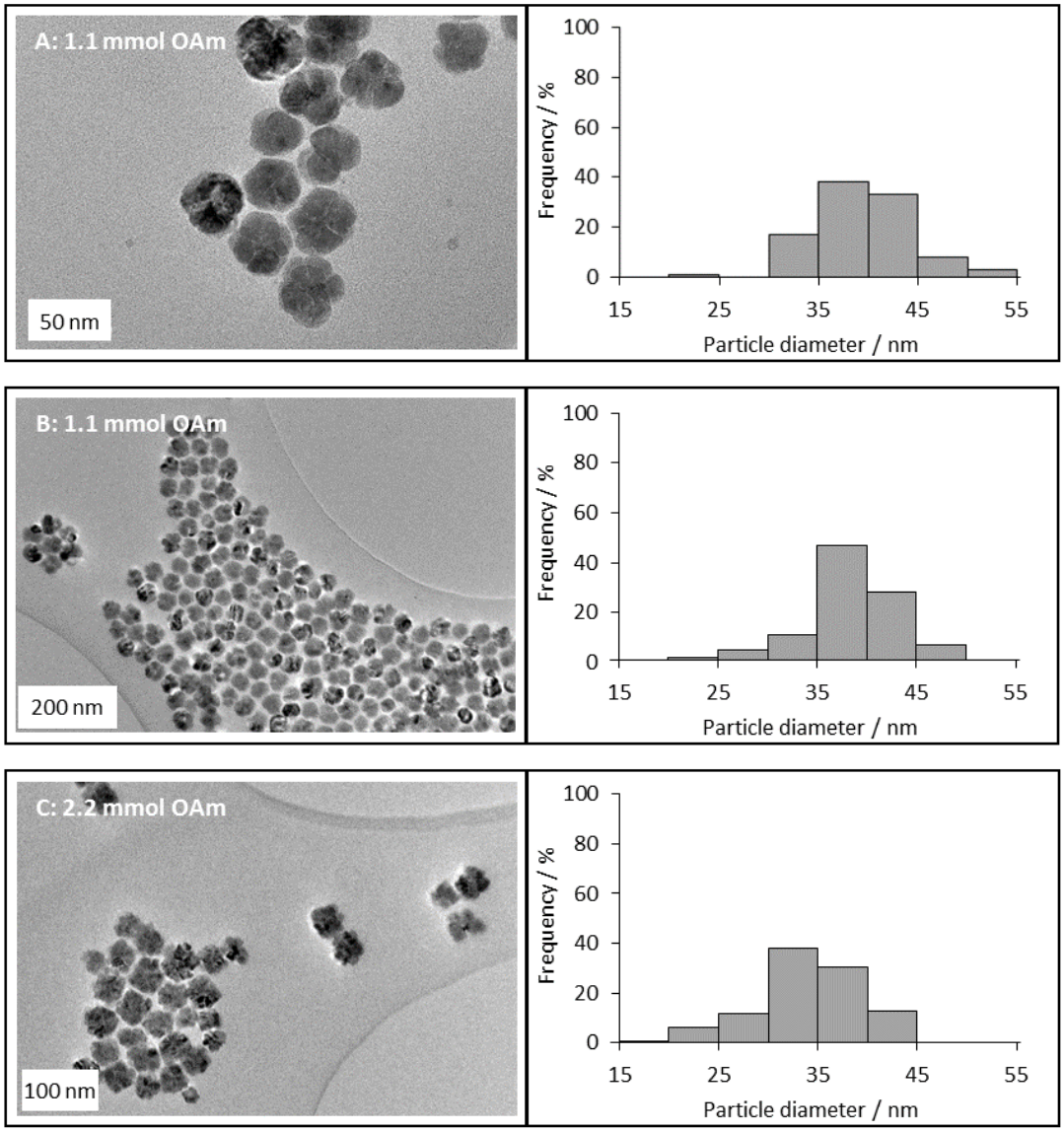

Figure 4.11. TEM images, and histograms calculated from measurement of particle diameter from TEM images for a minimum of 100 particles. For nanoparticles synthesised according to Section 2.2.1.5, with 0.23 mmol copper(II) acetylacetonate at 200 °C with the following oleylamine concentrations, and sample names (see Appendix) A-B) 1.1 mmol oleylamine (OAm) for Cu-031215_1, and Cu-120716_1 respectively, and C) 2.2 mmol oleylamine for Cu-010316_1.

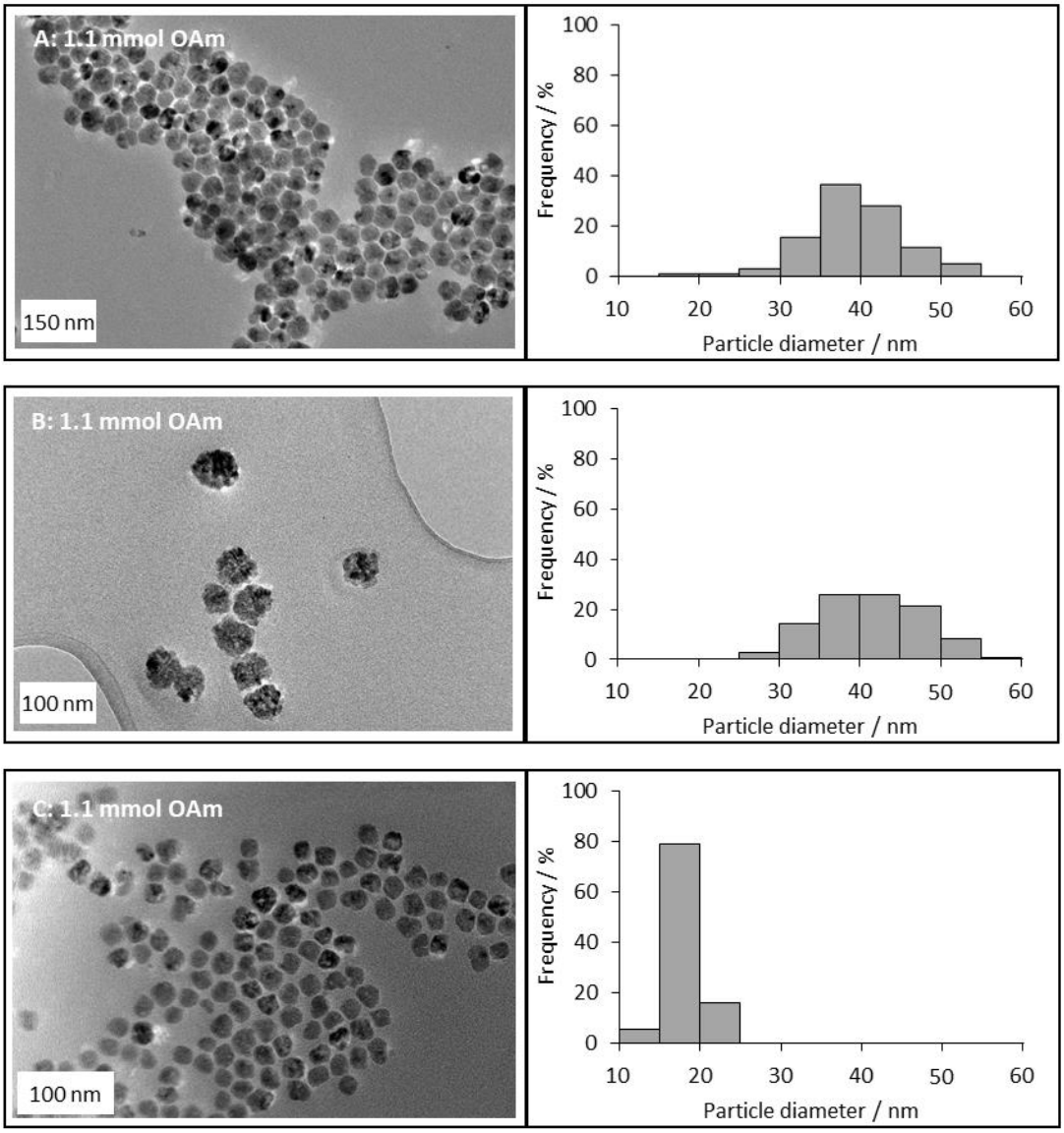

Figure 4.12. TEM images, and histograms calculated from measurement of particle diameter from TEM images for a minimum of 100 particles. For nanoparticles synthesised according to Section 2.2.1.5, for a 240 °C ripening temperature with 0.23 mmol copper(II) acetylacetonate with the following oleylamine (OAm) concentrations and sample names (see Appendix) A-C) 1.1 mmol oleylamine for Cu-020216_1, Cu-170216_1, and Cu-091215_1, respectively.

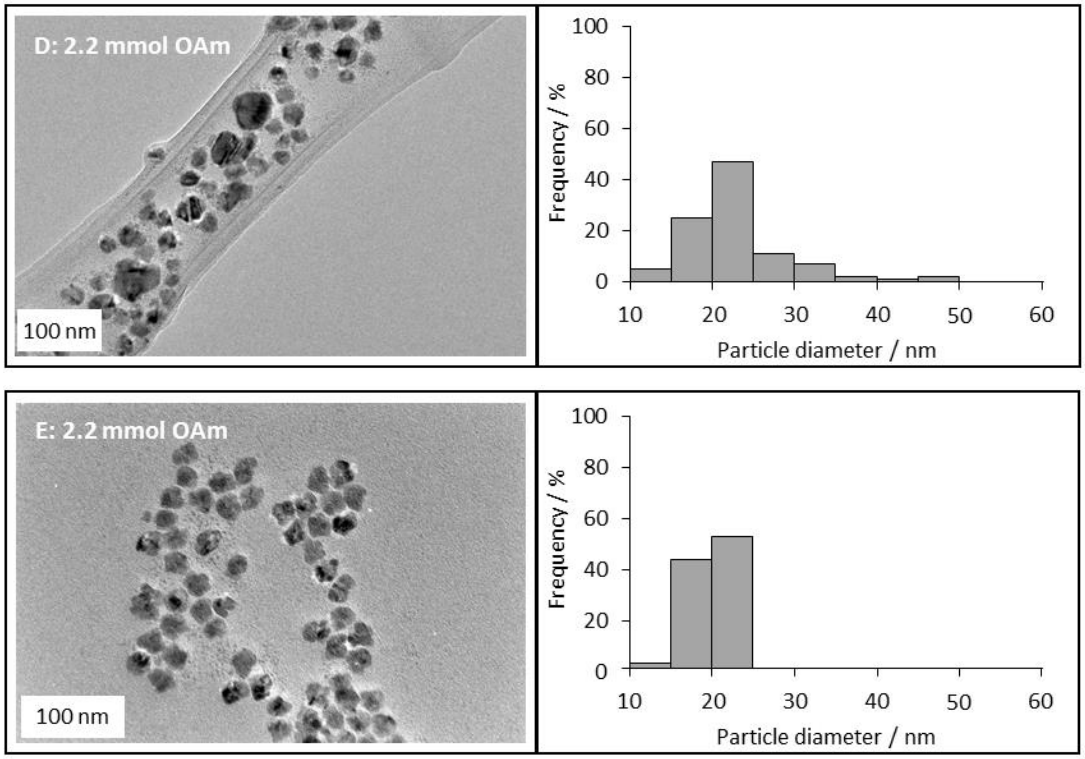

Figure 4.13. TEM images, and histograms calculated from measurement of particle diameter from TEM images for a minimum of 100 particles. For nanoparticles synthesised according to Section 2.2.1.5, for a 240 °C ripening temperature with 0.23 mmol copper(II) acetylacetonate with the following oleylamine (OAm) concentrations and sample names (see Appendix) D-E) 2.2 mmol oleylamine for Cu-181215_1, and Cu-220116_1 respectively.

4.1.1.2.2. Variation of capping agent: using combination of oleylamine and oleic acid

Figure 4.14 shows the effect, upon particle size, dispersity, and inductively coupled plasma-optical emission spectrometry (ICP-OES) yield, of oleic acid addition after the nanoparticle ripening stage. This constitutes a commonly utilised synthetic approach for synthesizing a range of nanoparticles.[16] Here oleic acid addition gave rise to very low yields by ICP-OES, compared to preparations under the same conditions in the absence of oleic acid. TEM images (Figure 4.14) showed the particles formed once oleic acid is added are varying shapes and sizes, unlike the spherical and relatively uniform oleylamine only capped nanoparticles. Addition of oleic acid after ripening is thought to cause displacement of the oleylamine due to the stronger interaction of the acid group compared to that of the amine.[16] However, it is possible that in the present case for the easily oxidised copper the acid may facilitate oxidation of the metal leading to dissolution of copper ions, which are washed out after synthesis, leading to a low yield by ICP-OES. Also examined was the effect of using both capping agents simultaneously as shown in Table 4.3. In one case (50/50 oleylamine:oleic acid) no particles at all were obtained (Table 4.3). TEM images (Figure 4.15) again showed particles with varying sizes and shapes when oleic acid capping agent was used compared to

oleylamine only capped nanoparticles. Using a very similar procedure in which both oleylamine and oleic acid capping agents were used at the same time, Mott *et al*. reported the synthesis of stable, monodisperse copper nanoparticles with sizes ranging from 5 to 25 nm.[7] It is assumed that the added reducing agent in their procedure in addition to any role during particle synthesis prevents the loss *via* oxidation and dissolution seen in the present study. Overall adding oleic acid did not improve control over the synthesis process but due to low yields of particles was found to be undesirable. Oleic acid was therefore not used in subsequent studies as a secondary capping agent.

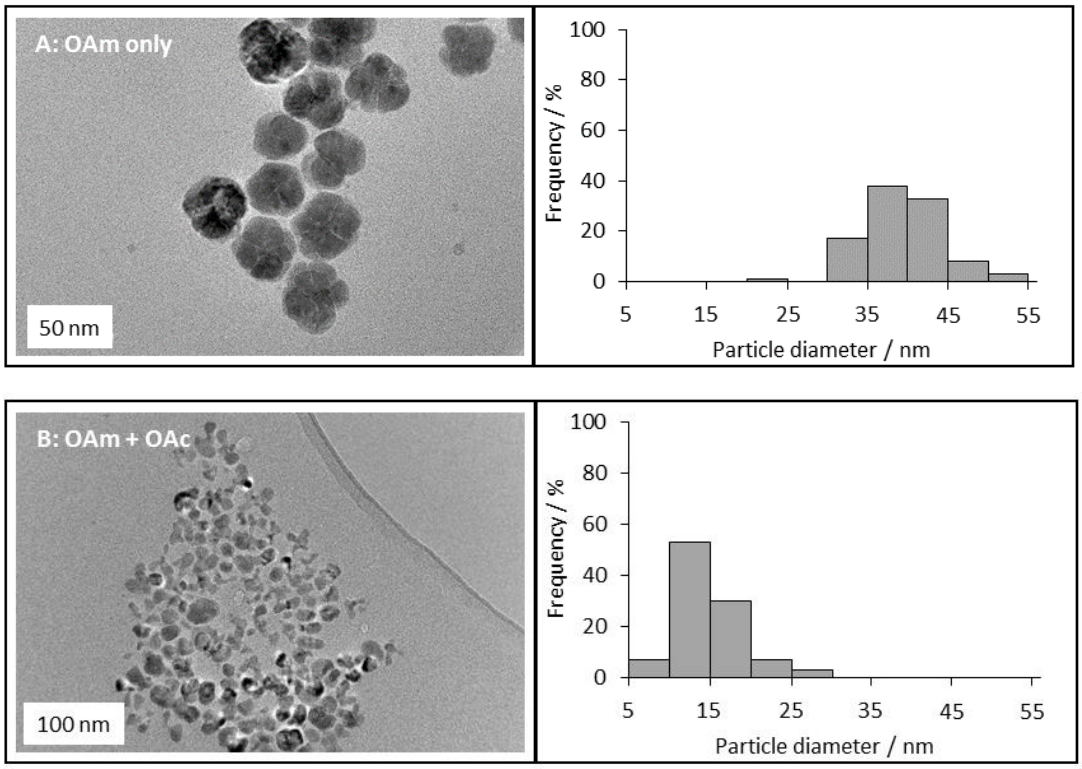

Figure 4.14. TEM images, and histograms calculated from measurement of particle diameter from TEM images for a minimum of 100 particles. For nanoparticles synthesised according to Section 2.2.1.5 with the following oleylamine (OAm) and oleic acid (OAc) concentrations with oleic acid added after ripening with oleylamine with the following sample names (see Appendix) of A) 1.1 mmol oleylamine Cu-031215_1, and B) oleylamine 0.71 mmol then oleic acid capping agent 0.38 mmol added after ripening, Cu-190716_1. Variation in the capping agent resulted in particle size distributions of 39 ± 5 nm, and 15 ± 4 nm for particles shown in images A and B respectively.

Table 4.3. Average particle size, and standard deviation for particles synthesised according to Section 2.2.1.5 with a mixture of oleylamine (OAm) and oleic acid (OAc) capping agents with both capping agents added at the same time. TEM images, particle size distributions and sample identifiers are given in Figure 4.14, with the exemption of the first data point Cu-230316_1 (with a molar concentration of oleylamine:oleic of 0.55:0.55 mmol) for which no particles were obtained after washing of the nanoparticle. †Note this sample is a repeat included to show reproducibility.

Concentration OAm / mmol	**Concentration OAc / mmol**	**Average particle size / nm**	**Standard deviation in particle size / nm**	**Standard deviation in particle size / %**	**%Cu nanoparticle yield (based on Cu ICP)**
0.55	0.55	n/a	n/a	n/a	n/a
0.99	0.11	9	6	67	9
1.1	0	39	5	13	n/a
1.1†	0	38	5	13	70

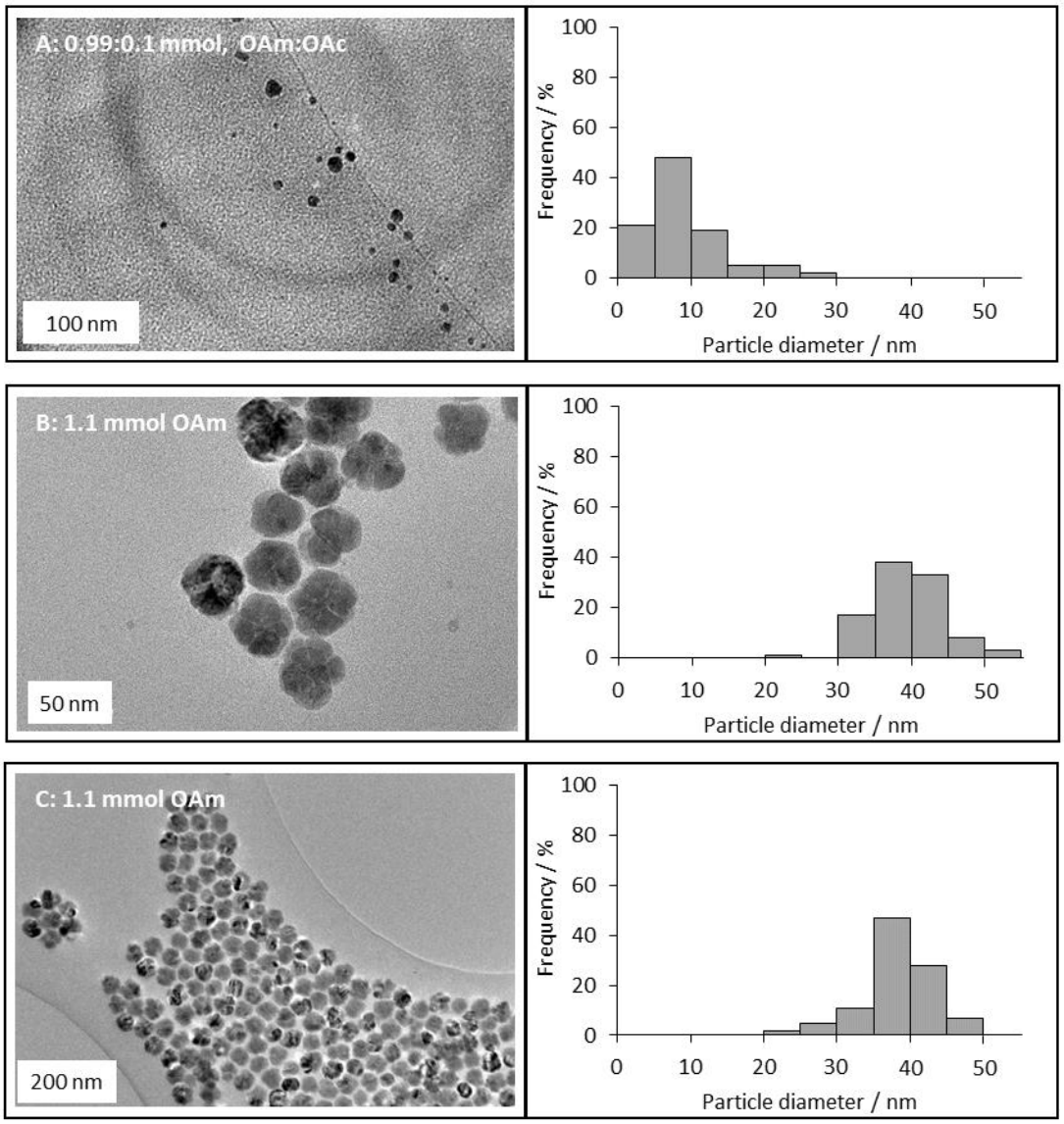

Figure 4.15. TEM images, and histograms calculated from measurement of particle diameter from TEM images for a minimum of 100 particles. For nanoparticles synthesised according to Section 2.2.1.5 with the following oleylamine (OAm) and oleic acid (OAc) concentrations with both capping agents added at the same time and sample names (see Appendix) of A) oleylamine 0.99 mmol and oleic acid 0.11 mmol Cu-240316_1, B-C)) 1.1 mmol oleylamine only, Cu -031215_1, and Cu-120716_1 respectively.

4.1.1.2.3. Comparison of oleylamine and octadecylamine capping agents

In order to investigate the possible role of the C=C double bond in oleylamine, the capping agent was replaced with the saturated analogue octadecylamine. As shown in Table 4.4, and Figure 4.16, the octadecylamine capping agent gave slightly differing particle sizes between the two batches synthesised, but particle size dispersity did not change significantly for batches or capping agents. Overall, particle shape and size was comparable for both capping agents.

Table 4.4. Average particle size, and standard deviation for particles synthesised according to Section 2.2.1.5 with oleylamine (OAm), and octadecylamine (ODA) capping agents in the absence of reducing agent. TEM images, particle size distributions and sample identifiers are given in Figure 4.16.

capping agent	particle size / nm	standard deviation / nm	standard deviation / %
OAm	39	5	13
OAm	38	5	13
ODA	33	4	12
ODA	52	6	12

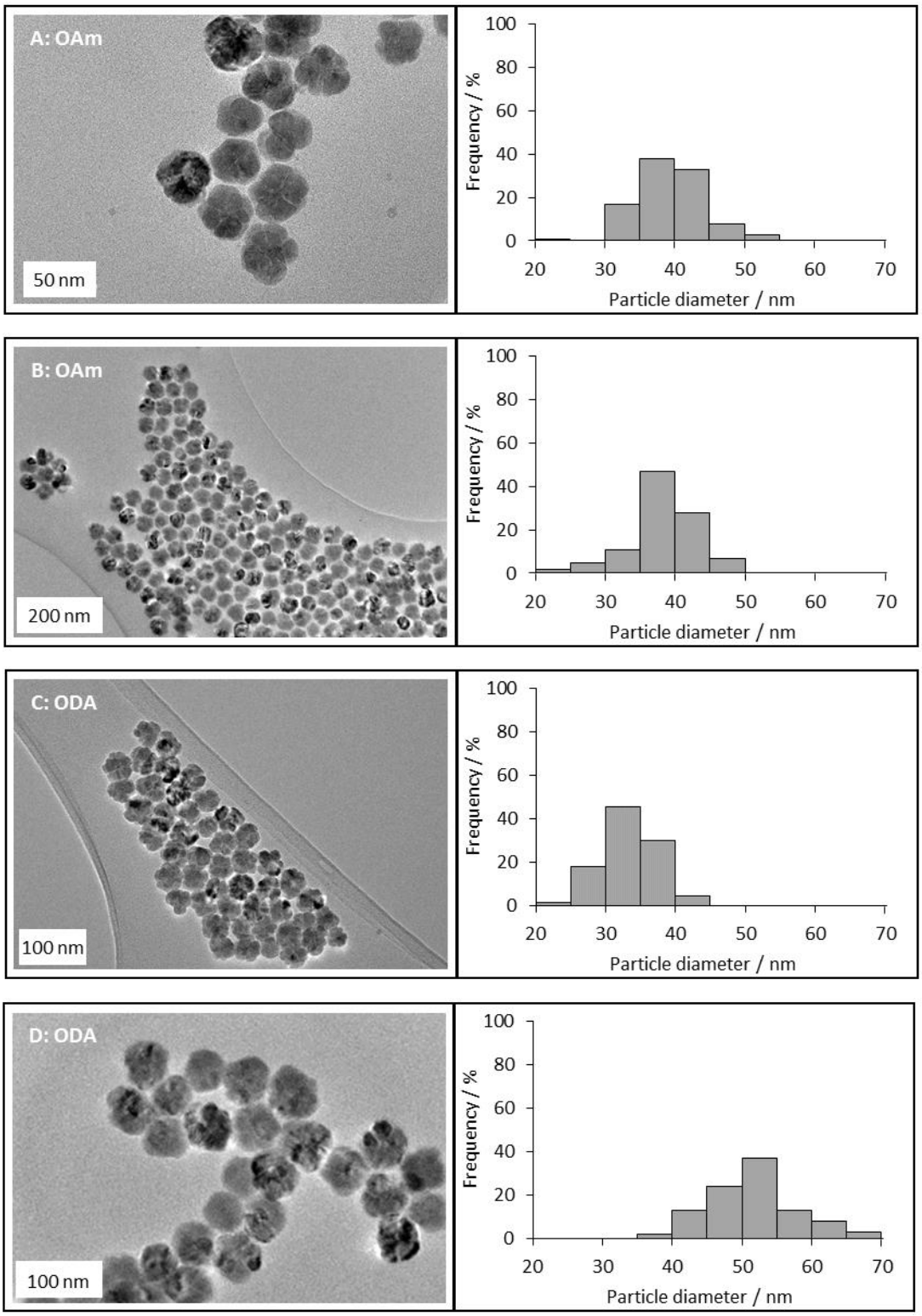

Figure 4.16. TEM images, and histograms calculated from measurement of particle diameter from TEM images for a minimum of 100 particles. For nanoparticles synthesised according to Section 2.2.1.5 in the absence of reducing agent, with the following capping agents, and sample names (see Appendix) of A-B) oleylamine (OAm) Cu-031215_1, and Cu-120716_1 respectively, C-D) octadecylamine (ODA), Cu-100216_1 and Cu-170616_1 respectively.

4.1.2. Monometallic copper nanoparticles by use of a separate reducing agent

Thermal reductions are commonly used in nanoparticle synthesis, and often rely upon the use of elevated reaction temperatures to achieve reduction of the metal salt (to the metal oxidation state) from oxidation of the solvent or other species that are available to act as reducing agents.[1,17,18] Reducing, coordinating capping agents such as oleylamine, which have a weak reducing effect can also be used.[3] However, reduction by this process is often slow, and so can lead to polydispersity in the particles formed. Therefore, addition of stronger reducing agents can be used to quickly facilitate reduction of the metal salt. This leads to fast nucleation which often leads to a more monodisperse particle distribution, as well as access to smaller particle sizes as a result of the formation of many more particles through rapid nucleation before growth can occur.[19]

4.1.2.1. Morpholine borane reducing agents

Morpholine borane was selected as a potential reducing agent based on the use of this and similar amine-borane complexes to form nanoparticles in the literature.[20–22] It is relatively easy to handle and readily available. Amine borane complexes have been suggested to have a dual role in nanoparticle synthesis, acting as a reducing agent, as well as providing additional stabilision.[23] It is known from differential scanning calorimetry (DSC) and thermogravimetric analysis (TGA) that thermal decomposition of borane-ammonia, BH_3NH_3, occurs through two distinct decomposition steps in the temperature range of 67 to 227 °C. This results in hydrogen release, and decomposition to mainly $(BH_2NH_2)_x$ type polymers.[24,25] Small amounts of borazine are also thought to be formed. More generally dehydrogenation of amino boranes is known to create BHN_x type polymers.[26–29] In the presence of the copper(II) ion (Cu^{2+}, provided from a copper(II) chloride starting material),[30] along with a range of other transition metals,[31–34] metal catalysed hydrolysis or methanolysis of amine-borane type complexes occurs with release of hydrogen. In the case of copper(II) chloride, the intermediate $[NH_4]^+[BCl_4]^-$ prevents borazine formation, giving hydrogen and polymer rather than network formation.[30] It is clear, therefore, that the hydrogen released could also indirectly act to reduce many metal salts (essentially those with a reduction potential greater than 0 V including the copper(II) ion), or the amine borane can react directly to reduce the metal salt. It has also been proposed that these aminoborane polymers, formed by thermal decomposition of the reducing agent, act to stabilise nanoparticles formed.[23] It may be desirable to avoid embedding the nanoparticles in a polymer network for applications where the colloidal nanoparticles are desired for use independently of the polymer. The use of a secondary amine such as morpholine should prevent the formation of such polymers.

Figure 4.17 shows the effect of conducting the synthesis in the absence of reducing agent, with the reducing agent now added to the preheated mixture, to which the metal salt is then added. From Figure 4.17 the addition of small amounts of morpholine borane reducing agent appears to have a limited effect on particle size and dispersity, with similar sizes being obtained to when it is absent. When a significant excess of reducing agent is used (assuming 1:1 stoichiometry), a dramatic decrease in particle size and dispersity was observed.

TEM images for the same samples are shown in Figures 4.18 and 4.19, indicating the expected coalesced and spherical particles formed in the absence of reducing agent or low concentrations of reducing agents. Figure 4.18 B and C (low and stoichiometric reducing agent) showed particles with a highly coalesced shape (comprising many smaller nanoparticles than before, as shown in Figure 4.18 C high magnification image), suggesting the possibility that a slight switch in mechanism takes place upon reducing agent addition, despite the limited change seen in particle size. In this regime nanoparticle growth by aggregation still clearly dominates. Figure 4.19 D, and E, with super-stoichiometric amounts of reducing agent, show particles with a more spherical shape and much smaller in size. It may be suggested that these small particles are the result of burst nucleation leading to the formation of many small particles, with the fact that all the metal is initially reduced leading to less gradual growth and particle changes in the subsequent time period. The observation that >1:1 morpholine borane complex:copper(II) acetylacetonate is required (but double results in small particles) suggests that either a large excess is required to achieve efficient reduction or else the mechanism requires two equivalents of reducing agent present, see the discussion below.

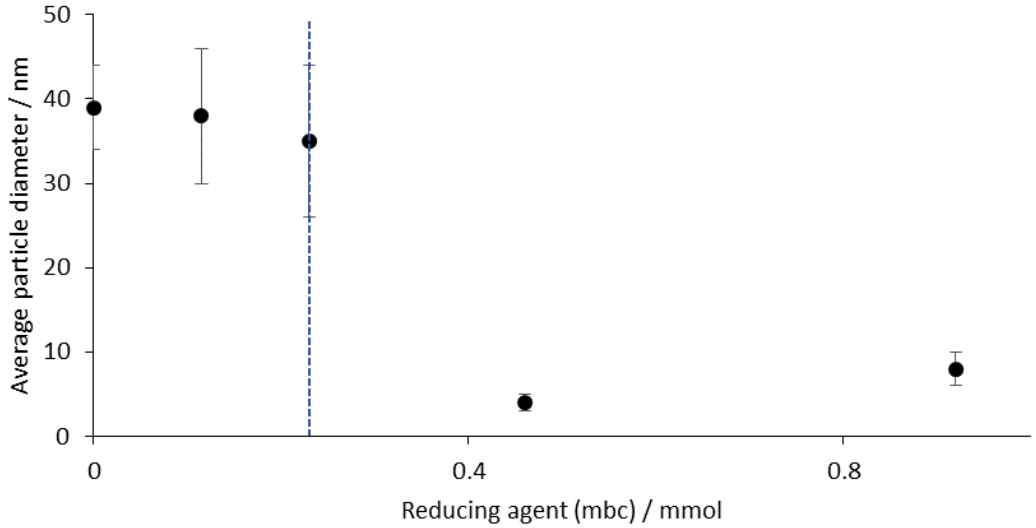

Figure 4.17. Average particle size, and standard deviation for particles synthesised according to Section 2.2.1.5 in the presence of varying amounts of morpholine borane complex (mbc) for 0.23 mmol copper(II) acetylacetonate, oleylamine reducing agent for preparation at 200 °C. TEM images, particle size distributions, and sample identifiers are given in Figures 4.18 and 4.19. Error bars shown represent the standard deviation in particle diameter measured for a minimum of 100 particles. The blue dashed line represents a stoichiometric ratio of copper(II) acetylacetonate to morpholine borane complex.

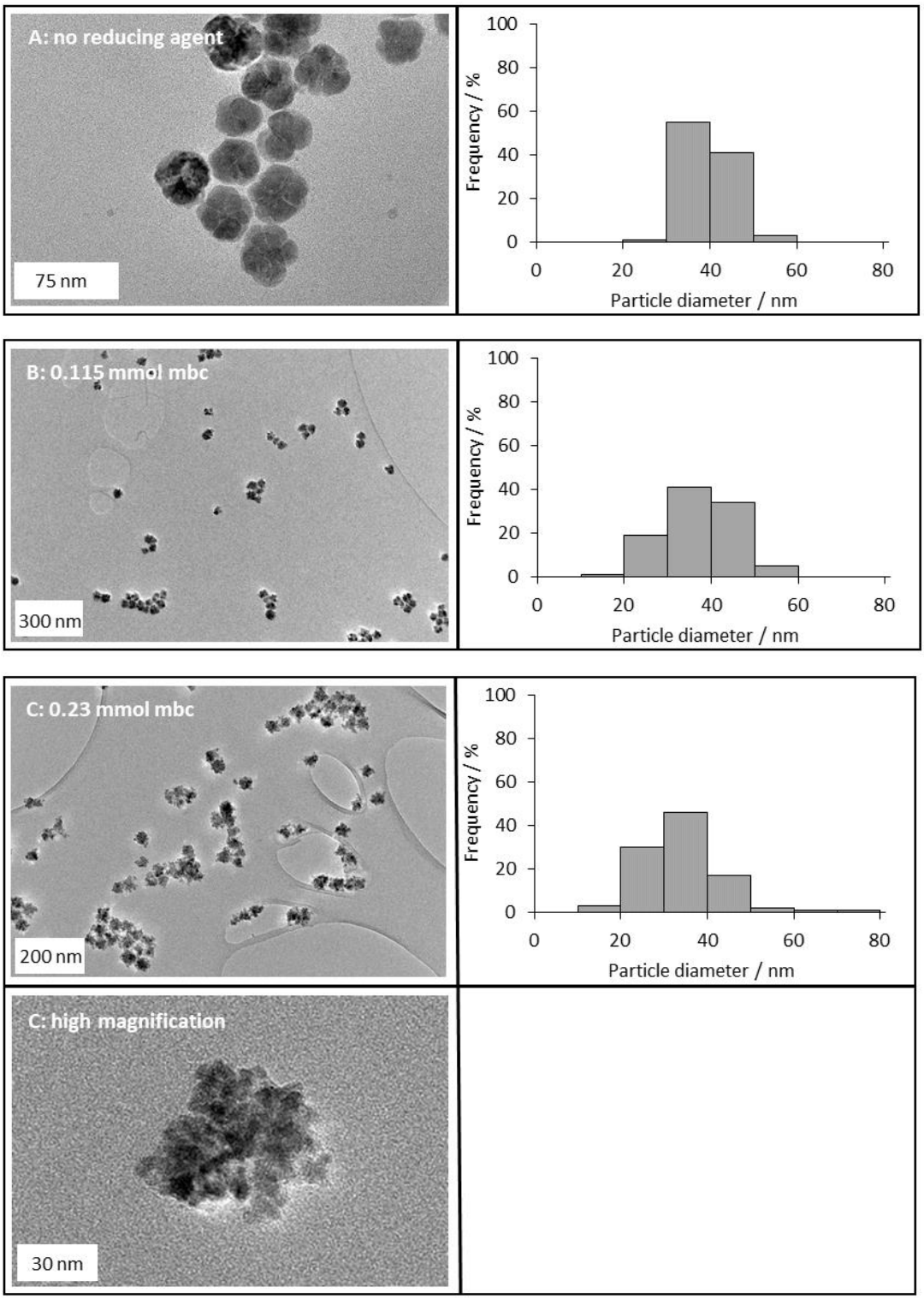

Figure 4.18. TEM images, and histograms calculated from measurement of particle diameter from TEM images for a minimum of 100 particles. For nanoparticles synthesised according to Section 2.2.1.5 with 0.23 mmol copper(II) acetylacetonate, and with the following concentrations of morpholine borane complex (mbc), and sample names (see Appendix) of A) no morpholine borane complex Cu -031215_1, B) 0.115 mmol morpholine borane complex Cu-240616_1, C) 0.23 mmol morpholine borane complex Cu-040516_1. For C a high magnification image is given in order to show the coalesced nature of the particles.

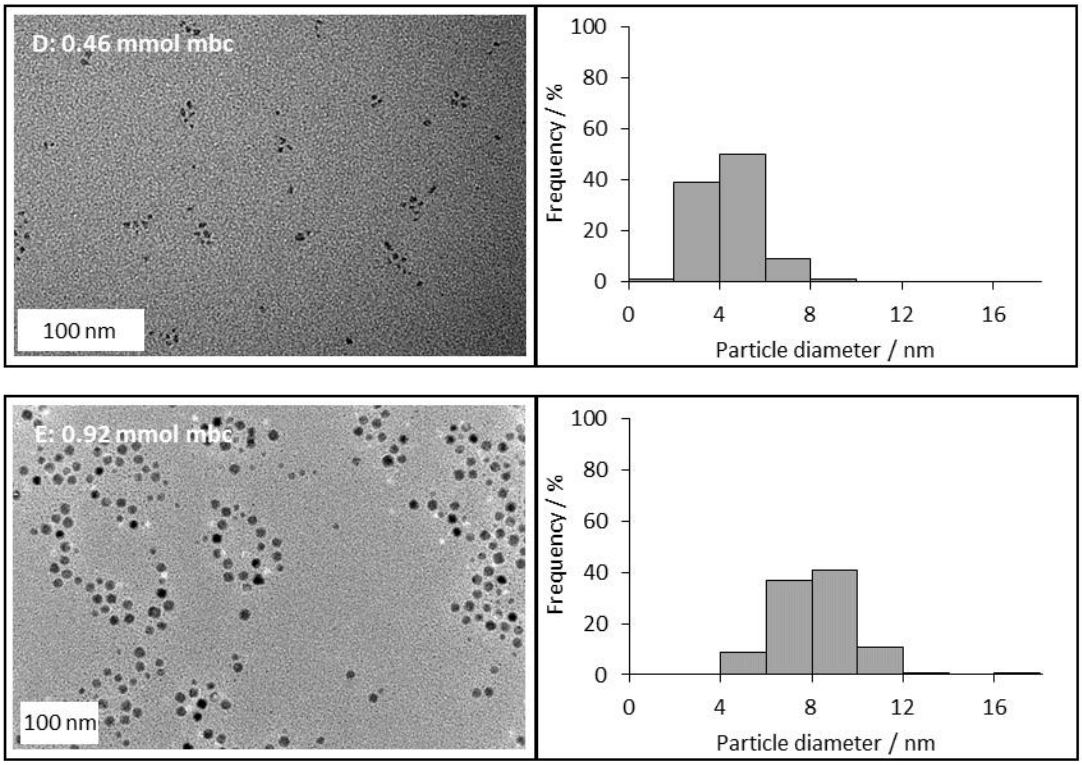

Figure 4.19. TEM images, and histograms calculated from measurement of particle diameter from TEM images for a minimum of 100 particles. For nanoparticles synthesised according to Section 2.2.1.5 with 0.23 mmol copper(II) acetylacetonate, and with the following concentrations of morpholine borane complex (mbc), and sample names (see Appendix) of D) 0.46 mmol morpholine borane complex Cu-060516_1, E) 0.92 mmol morpholine borane complex Cu-140716_1.

4.1.2.1.1. Mechanistic studies of morpholine borane reducing agent *via* DSC and ^{11}B nuclear magnetic resonance (NMR) spectroscopy

Attempts to examine the mechanism of metal nanoparticle formation using amine-borane complexes have been made by Lidor-Shalev and Zitoun using acetylacteonate metal precursors.[19] They examined tin acetylacetonate in the absence of capping agent, and found that increasing the amount of amine-borane reducing agent gave larger particle sizes. This led the authors to suggest a growth controlled kinetic regime. This would contrast the apparent nucleation controlled scheme shown within our copper system, where more amine-borane reducing agent caused dramatic reduction in nanoparticle size. The authors noted that in their case addition of a capping agent, hexadecylamine, had no significant effect on particle size but did reduce particle dispersion. On the basis of DSC and ^{11}B NMR spectroscopy they suggested (with limited evidence) that the reduction followed the mechanism given in Figure 4.20: a hydride intermediate is formed by the reaction of the amino-borane and acetylacetonate, leading to nanoparticle formation.

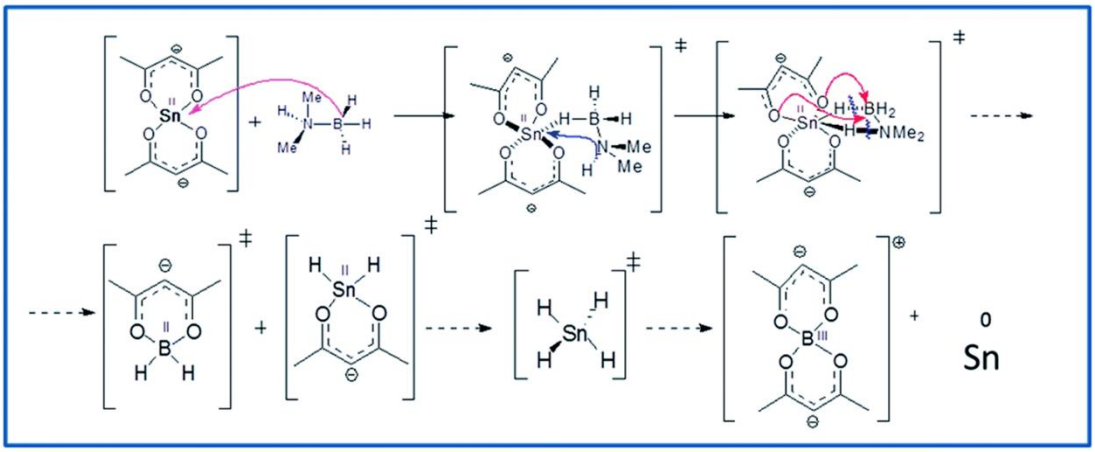

Figure 4.20. Reaction mechanism for amine-borane and tin acetylacetonate leading to nanoparticle formation. Reproduced (in part) from {Lidor-Shalev, O. & Zitoun, D. Reaction mechanism of 'amine–borane route' towards Sn, Ni, Pd, Pt nanoparticles. RSC Adv 4, 63603–63610 (2014).} with permission of The Royal Society of Chemistry.

To investigate further the mechanism of the copper acetylacetonate system ^{11}B NMR and DSC were conducted analogous to those performed for the case of tin discussed above. DSC of pure morpholine borane, shown in Figure 4.21 Spectra 1, gave an endotherm around 93 °C, corresponding to the expected melting point range of 93-97 °C.[35,36] Additionally an endotherm centred around 170 °C must result from decomposition of the amine-borane, possibly attributable to the morpholine borane dimer forming with release of hydrogen. Mixing of morpholine borane complex and copper(II) acetylacetonate in two differing mass ratios (Figure 4.21 Spectra 2, and 3 *2.6:1* and 4.9:1 molar ratio of morpholine borane to copper(II) acetylacetonate, respectively) gave an exotherm in both cases. This exotherm centred at 93 °C was attributed to the reaction of morpholine borane and copper(II) acetylacetonate leading to the formation of copper metal. An endotherm was also seen in both cases centred around 95 °C. The intensity of this endotherm increased with higher morpholine borane:copper acetylacetonate concentrations as expected for decomposing excess morpholine borane (which presumably is now catalysed by the copper particles formed and so occurs at lower temperatures than in A).

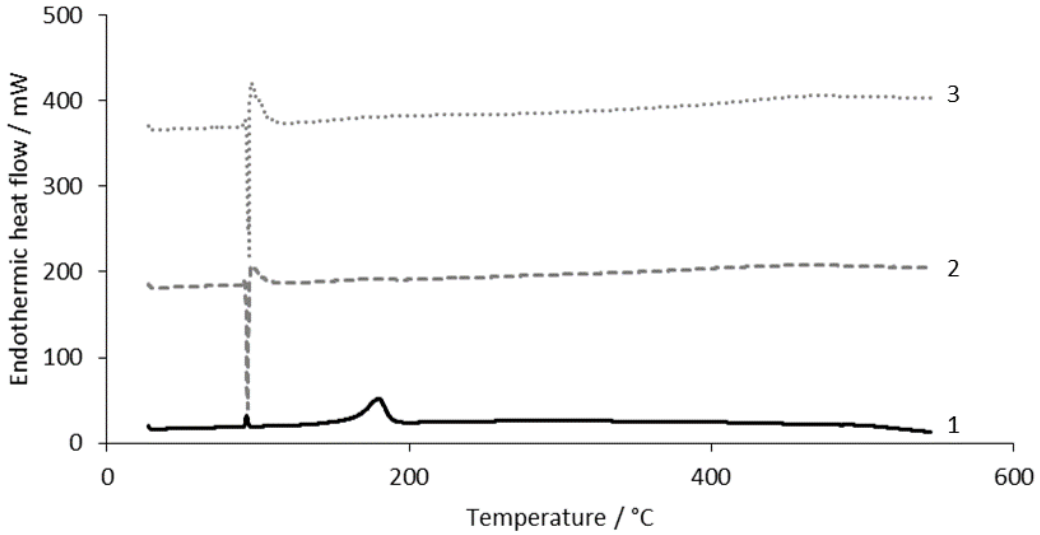

Figure 4.21. DSC for 1- pure morpholine borane complex, 2- 2.6 : 1 molar ratio of morpholine borane to copper(II) acetylacetonate, 3- 4.9:1 molar ratio of morpholine borane to copper(II) acetylacetonate. All data has been offset for clarity.

^{11}B NMR spectra of the crude reaction product is given in Figure 4.22. Broad features were seen for the empty glass NMR tube, attributed to borosilicate in the glass. A sharp peak was seen at 17.5 ppm for the crude reaction mixture, and this was attributed to the decomposition product of the morpholine borane as some sort of oxygen containing species, such as that suggested in Figure 4.20, $B(acac)_2^+$. The assignment was made due to the similarity of the chemical shifts to Lidor-Shalev and Zitoun,[19] although their assignment of this precise species is unclear. This is in line with the proposed reduction mechanism, for the amine-borane complex.

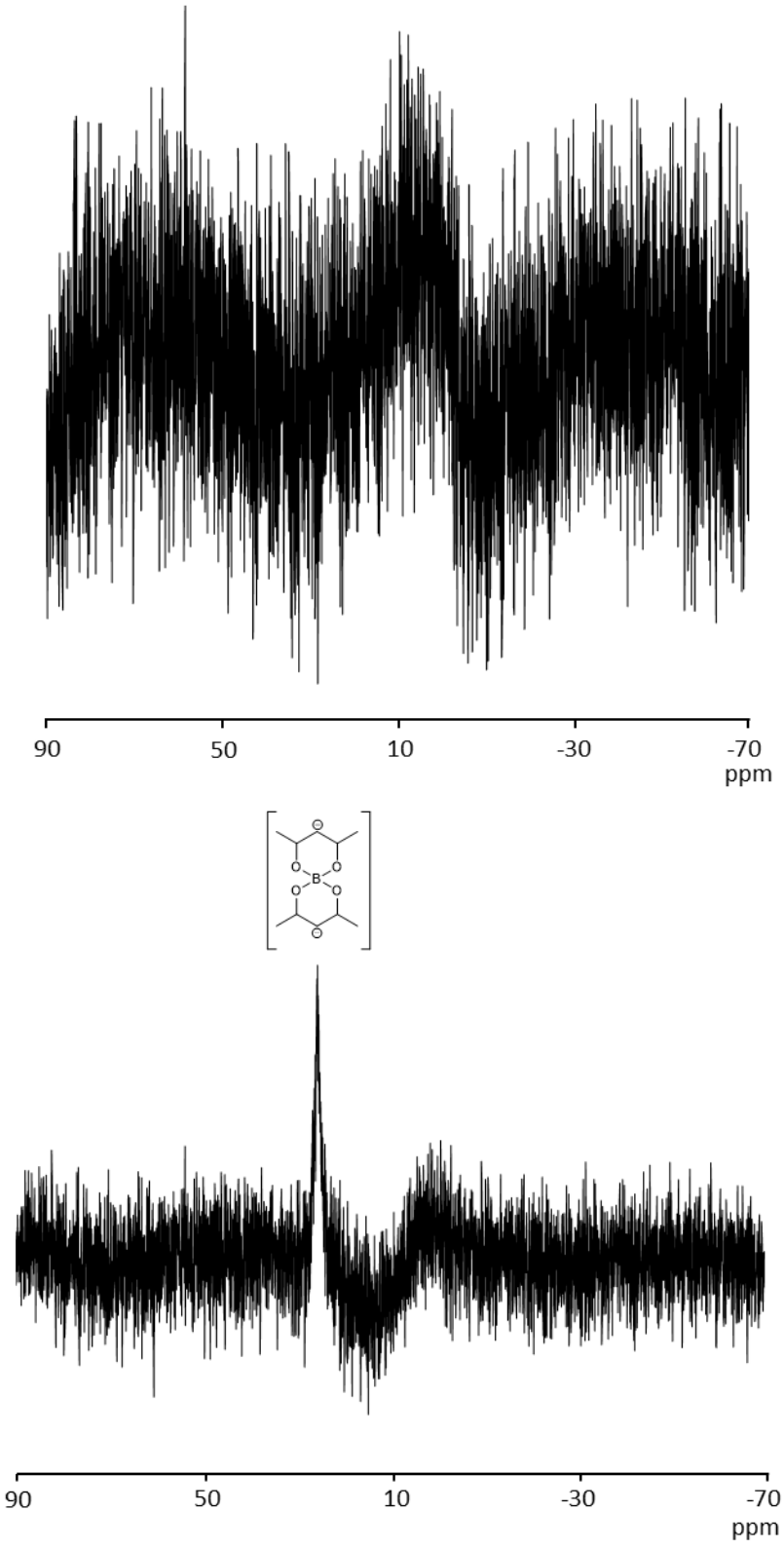

Figure 4.22. ^{11}B NMR for top- empty glass tube, bottom- reaction mixture in the glass tube.

4.1.2.1.2. Morpholine borane reducing agent with octadecylamine capping agent

Figure 4.23 shows that octadecylamine, used with morpholine borane reducing agent, appears to give tighter size distributions than for particles capped with oleylamine. Smaller

particles were also seen, and are interestingly now accessed with lower amounts (0.23 mmol) of morpholine borane complex, although larger amounts of reducing agent still appeared to narrow the size distribution.

Addition of 0.23 mmol of reducing agent significantly decreases the particle size, and the highest amount of reducing agent (0.92 mmol) produced the smallest particles. The ability to synthesise smaller particles, with less morpholine borane complex is seen, although between 0.23 mmol and 0.92 mmol no clear correlation between amount of reducing agent, and particle size was seen.

TEM images (Figures 4.24, and 4.25) show a clear change in particle appearance from coalesced (image A, B), to roughly spherical (image C-E). There was no indication of coalescence upon morpholine borane addition (images C-E), and no significant change in shape for variation of reducing agent concentration. The poorer control obtained for the 1:1 ratio of morpholine borane:copper(II) acetylacetonate suggests that although with octadecylamine better control is obtained (possibly as a result of more effective capping), still complete reduction did not occur efficiently at the start of the reaction. It can be speculated that octadecylamine is better for templating the small particles in the presence of reducing agent, although further repetitions are needed to confirm this and no mechanistic explanation can currently be given.

The alkene functionality in oleylamine has been proposed as a possible secondary adsorption site, capable of interacting with the metal and providing further stabilisation. Further stabilisation might be expected to allow access to smaller nanoparticles, with inherently higher surface areas. This idea however does not fit with the trend observed here that oleylamine is slightly less effective as a capping agent than octadecylamine.

Overall, the reduction process is broadly similar with good size control of small nanoparticles being obtained for a 2:1, reducing agent:metal salt ratio in both cases.

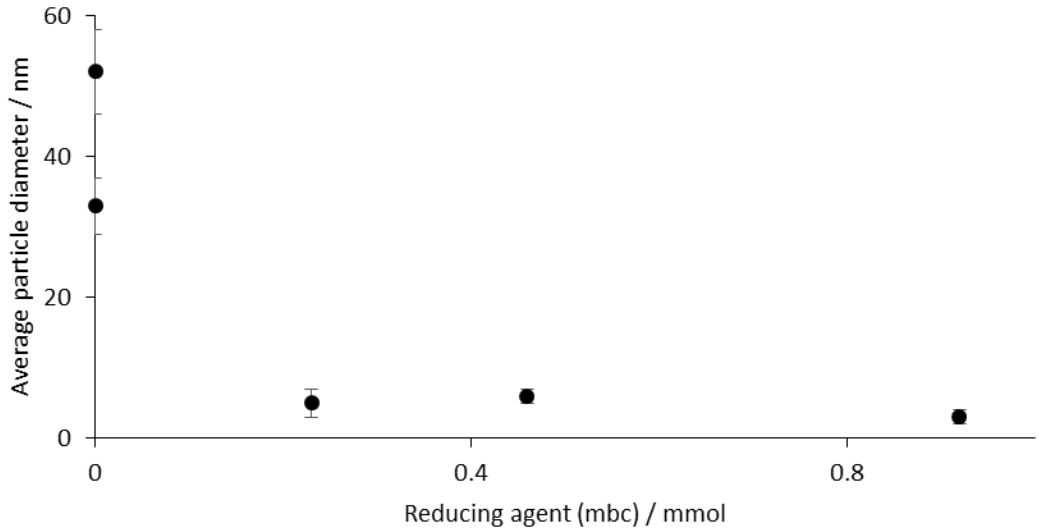

Figure 4.23. Average particle size, and standard deviation for particles synthesised according to Section 2.2.1.5 in the presence of varying amounts of morpholine borane complex (mbc), and octadecylamine capping agent for 0.23 mmol copper(II) acetylacetonate. TEM images, particle size distributions, and sample identifiers are given in Figures 4.24 and 4.25. Error bars shown represent the standard deviation in particle diameter measured for a minimum of 100 particles.

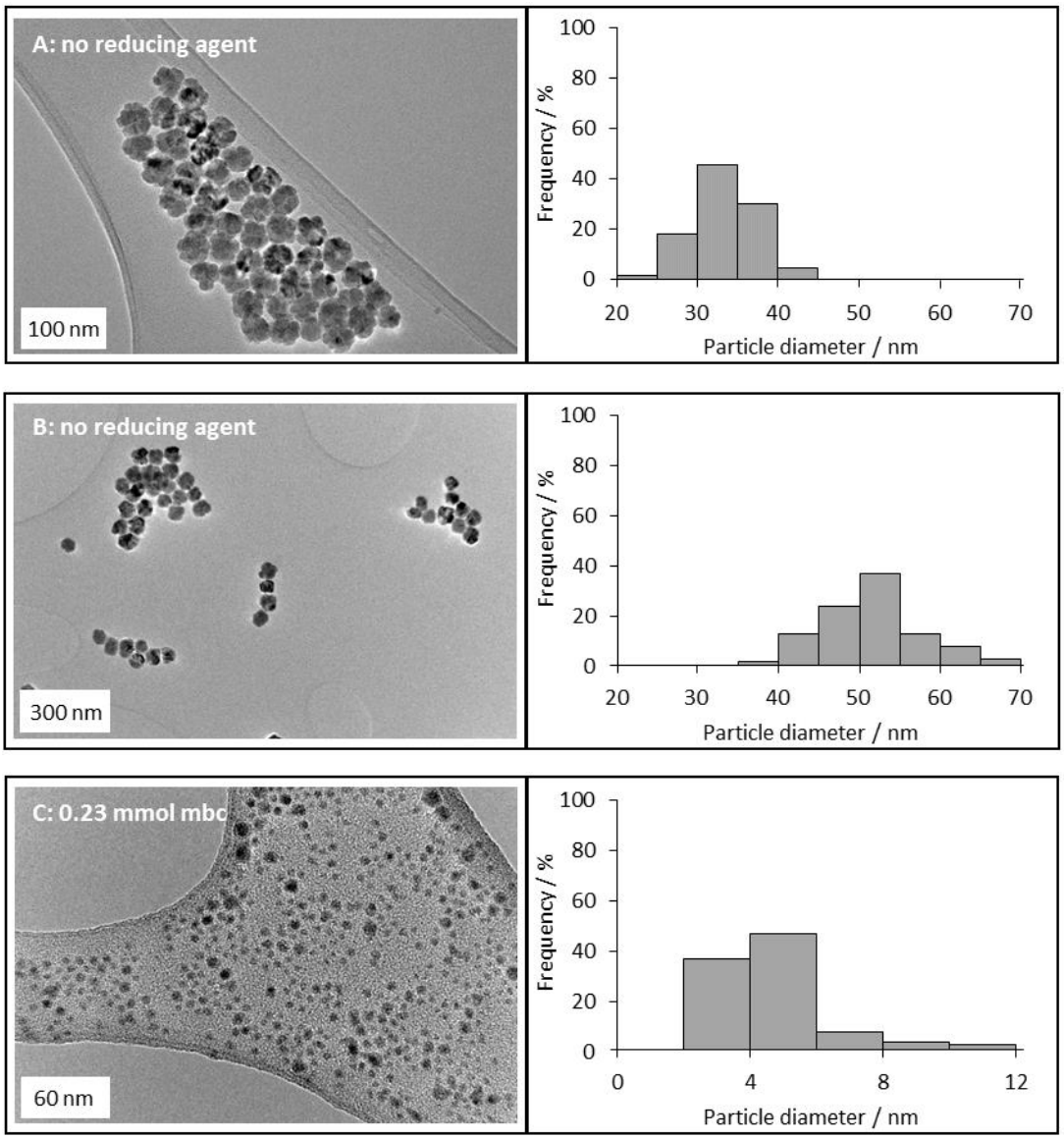

Figure 4.24. TEM images, and histograms calculated from measurement of particle diameter from TEM images for a minimum of 100 particles. For nanoparticles synthesised according to Section 2.2.1.5 for octadecylamine capping agent with 0.23 mmol copper(II) acetylacetonate with the following concentrations of morpholine borane complex (mbc) and sample names (see Appendix) of A-B) no morpholine borane complex Cu-100216_1, and Cu-170616_1 respectively, C) 0.23 mmol morpholine borane complex Cu-310316_1.

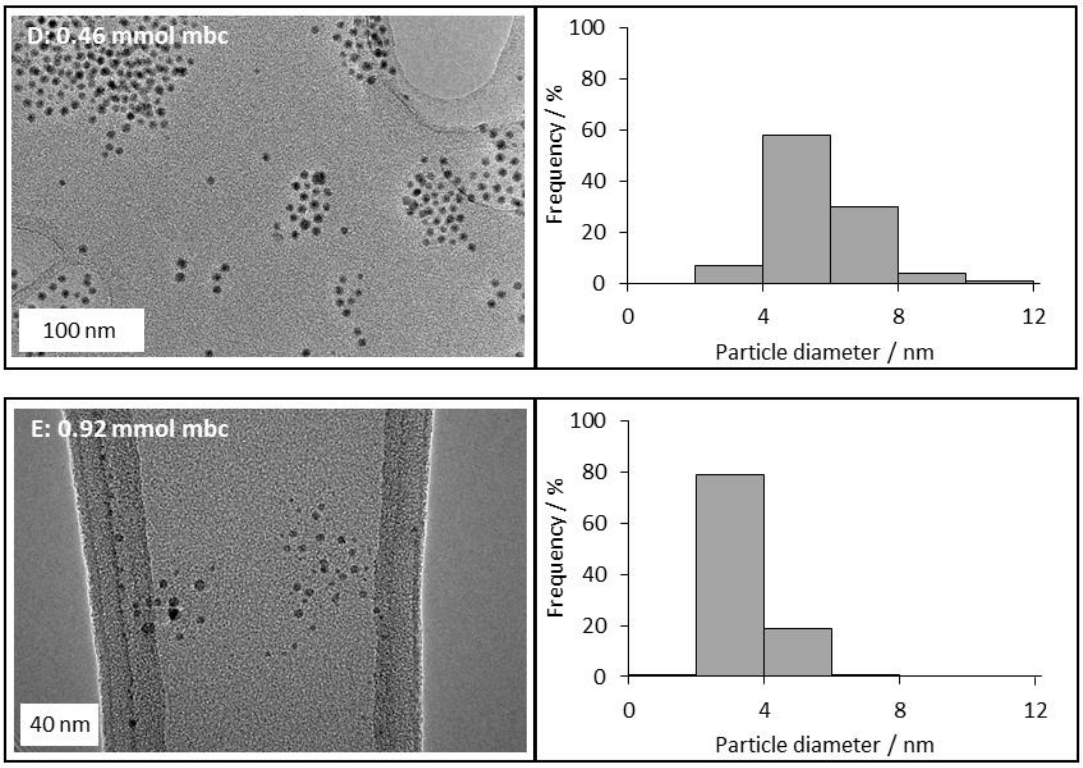

Figure 4.25. TEM images, and histograms calculated from measurement of particle diameter from TEM images for a minimum of 100 particles. For nanoparticles synthesised according to Section 2.2.1.5 for octadecylamine capping agent with 0.23 mmol copper(II) acetylacetonate with the following concentrations of morpholine borane complex (mbc) and sample names (see Appendix) of D) 0.46 mmol morpholine borane complex Cu-150716_1, E) 0.92 mmol morpholine borane complex Cu-190716_2.

4.1.2.2. 1,2-tetradecandiol reducing agent

A weaker none amine-borane based reducing agent, 1,2-tetradecandiol, was investigated to further understand the role of the reducing agent, and provide an example analogous to the work by Mott *et al.* which used a similar diol.[7] The particle size results for syntheses using this reducing agent are shown in Figure 4.26 and the corresponding TEM images in Figure 4.27. As before, addition of very small amounts of reducing agent (0.023 mmol) gave little change in particle size and distribution. However, upon addition of stoichiometric amounts of reducing agents very large particles (100's of nm) were formed. Examination of the TEM images, shown in Figure 4.27, shows various sizes of very large strongly shaped particles are formed, suggesting equilibration of low or favoured surface energy facets (possibly influenced by solution additives including the reducing agent or its oxidation products adsorbed on the particle surface). The large particles formed suggest no burst nucleation occurs (unlike with amine borane), and instead the reducing agent contributes to the steady growth of very large particles. In the presence of a weak reducing agent additional nucleation

during the growth stage can occur, as not all of the metal is reduced initially. This type of mechanism has been known to produce large polydisperse particles of this type.[37]

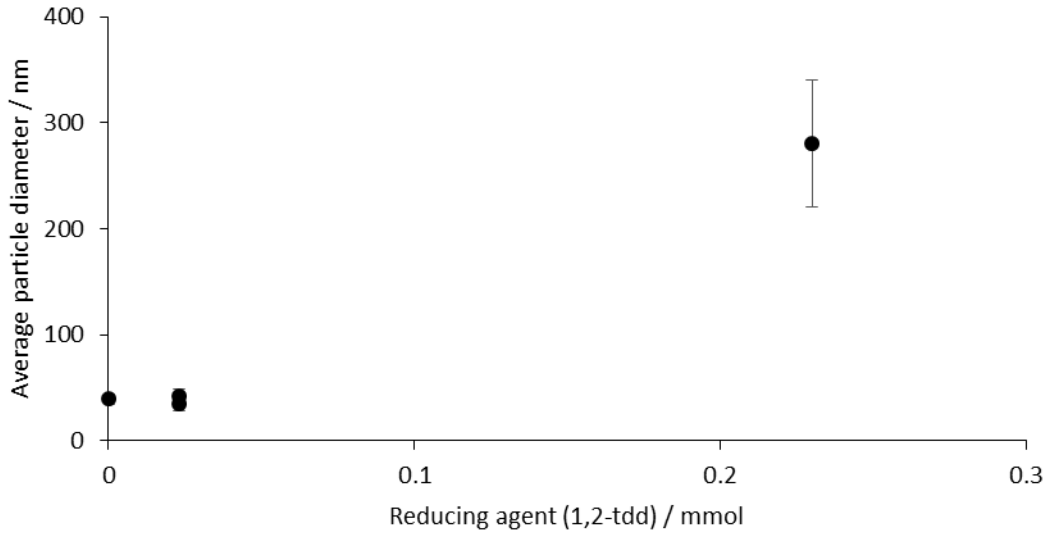

Figure 4.26. Average particle size, and standard deviation, for particles synthesised according to Section 2.2.1.5 in the presence of varying amounts of 1,2-tetradecanediol (1,2-tdd) for 0.23 mmol copper(II) acetylacetonate. TEM images, particle size distributions, and sample identifiers are given in Figure 4.27. Error bars shown represent the standard deviation in particle diameter measured for a minimum of 100 particles.

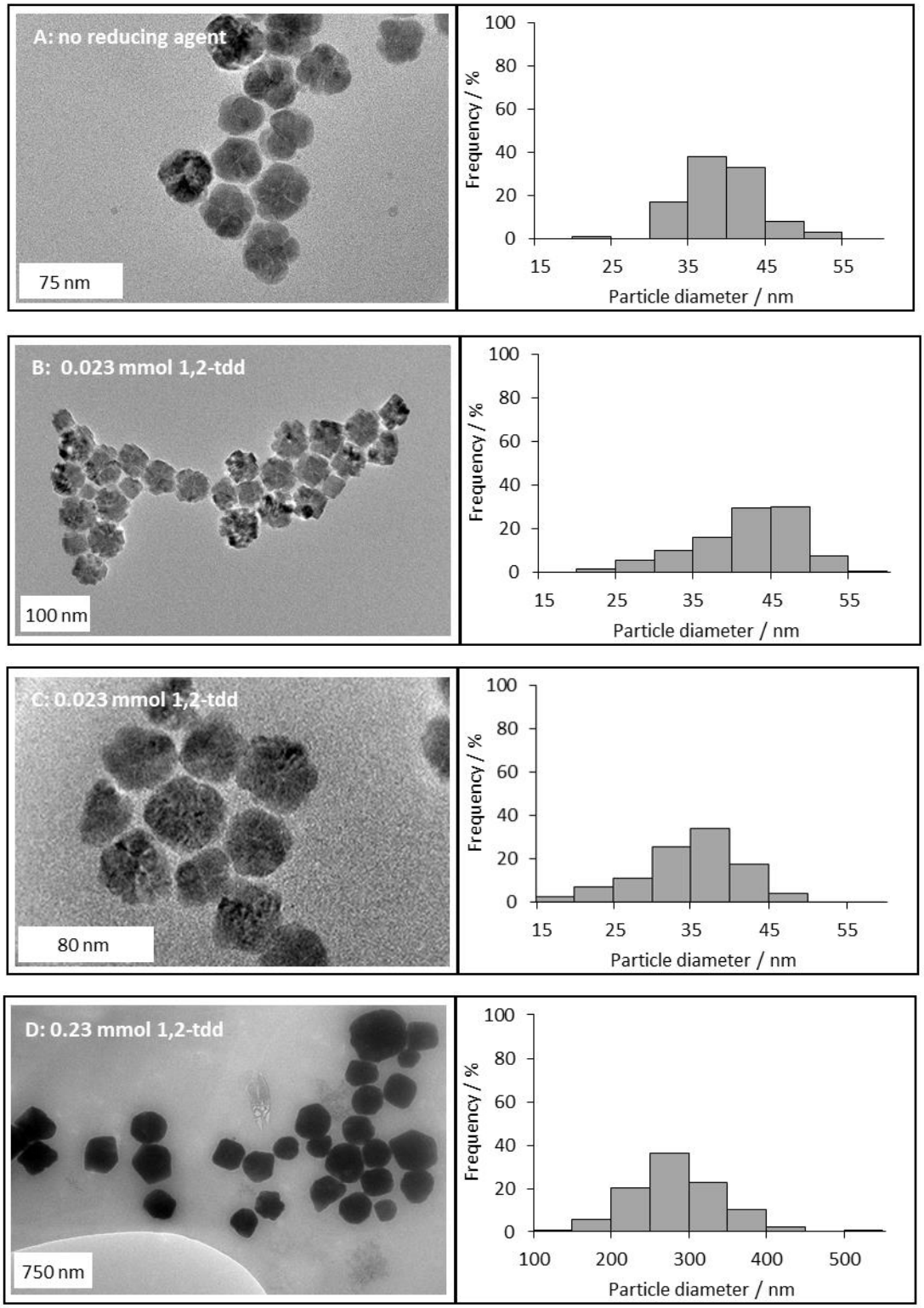

Figure 4.27. TEM images, and histograms calculated from measurement of particle diameter from TEM images for a minimum of 100 particles. For nanoparticles synthesised according to Section 2.2.1.5 with 0.23 mmol copper(II) acetylacetonate with the following concentrations of 1,2-tetradecanediol (1,2-tdd) and sample names (see Appendix) of A) no reducing agent Cu -031215_1, B-C) 0.023 mmol 1,2-tetradecanediol for Cu-040216_1, and Cu-110216_1 respectively, D) 0.23 mmol 1,2-tetradecanediol Cu-260216_1.

4.1.3. Infrared (IR) studies into the role of pyridine in the reduction of copper(II) acetylacetonate

During the nanoparticle synthesis, in order to now incorporate a reducing agent, the copper salt was added to the solution once at temperature and the solvation of copper(II) acetylacetonate in pyridine allowing for fast addition of the metal salt to the reaction mixture (typically comprised of capping agent, reducing agent, and high boiling point solvent typically at temperature). Copper(II) acetylacetonate was only sparingly soluble in most other organic solvents. As small a volume of pyridine as possible was used. This was to reduce the volume of vapour released, as the pyridine (boiling point 115 °C) was added to the typically 200 °C solution.

While it was assumed the pyridine should mostly be lost as vapour very rapidly, the possibility that pyridine might play a role in the reduction of the copper(II) acetylacetonate or subsequent particle growth cannot be excluded. To understand if pyridine was playing such a role, Fourier Transform (FT)IR spectroscopy was used to investigate if pyridine was remaining in the solution during the reaction. The use of complexed material did not need an additional solvent, for the copper(II) acetylacetonate as it was placed directly into the reaction mixture. This allowed direct comparison of FTIR spectra for copper nanoparticles synthesised both with and without pyridine.

From Figure 4.28 it can be seen from the FTIR spectra, that the same peaks were seen for copper nanoparticles synthesised both with (spectra B) and without pyridine (spectra A). For nanoparticles synthesised with pyridine FTIR spectroscopy was conducted after washing of the nanoparticles to remove any free pyridine. The intensity of the peaks does, however, differ between the two spectra. Assignments of all vibrational modes are given in Table 4.5. From this it can be seen that bands attributed to free and bound pyridine, reduce significantly in intensity for spectra A, as might be expected as no pyridine was used in this preparation. Vibrational modes assigned to oleylamine were also higher in intensity for spectra A given the complexation in oleylamine overnight this was not unexpected.

The presence of the bound pyridine, C-N-C coordinated bend at 636 cm^{-1}, was seen for spectra B This might indicate interaction of the pyridine, due to its being bound to the final nanoparticle. Whether this facilitates reduction is unknown, but interaction cannot be ruled out.

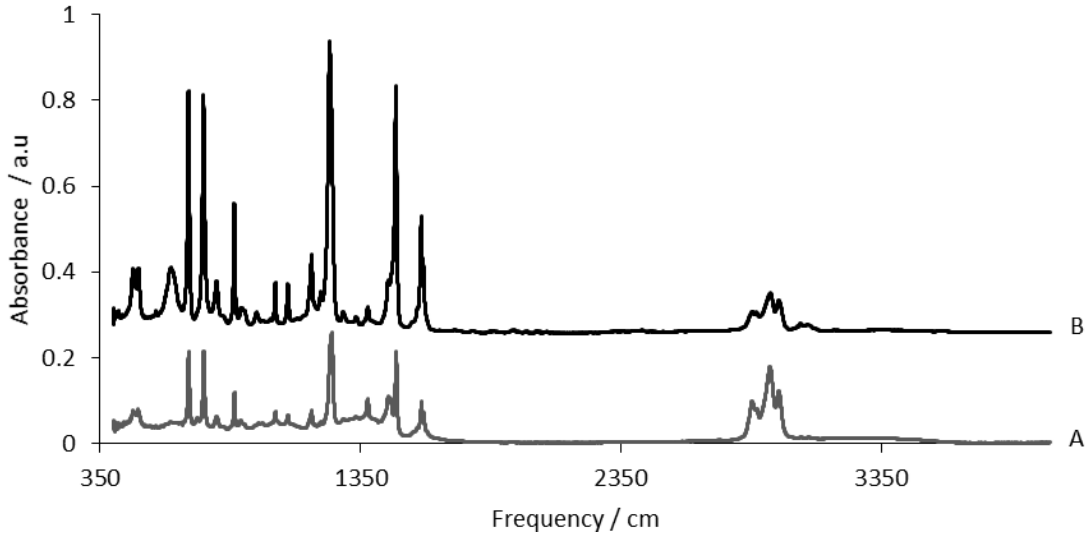

Figure 4.28. FTIR spectra for copper nanoparticles (hexane evaporated off till dryness) synthesised A) without pyridine B) for synthesis with pyridine, and after washing of the nanoparticles (see Section 2.2.1.5 for further details).

Table 4.5. Literature values for expected IR stretching frequencies for copper nanoparticles. Where sym str=symmetrical, asym=asymmetrical, str=stretch, v=vibration, def=deformation wagg=wagg. Numbers 1 to 4 denote assignment of the bands, 1 being assigned to oleylamine,[38,39] 2 for diphenyl ether,[40,41] 3 for free pyridine,[42] 4 for bound pyridine.[43]

Vibrational mode	Frequency / cm^{-1}
NH_2 v-asym and NH_2 v-sym[1]	3376, 3300
=C-H v-bend[1]	3006
CH v-asym and CH v-sym[1]	2922, 2854
-C=H v-bend[1]	1647
NH_2 v-bend[1]	1593, 795
CH_3 v-bend[1]	1465
C-N v-bend[1]	1071
C-C v-bend[1]	722
O-C-O sym str[2]	1231
$C_\beta HC_\gamma H$ def[3]	1147
$C_\gamma H$ def, $C_\alpha H$, $C_\beta H$ sym str def[3]	1089
$C_\alpha H$, $C_\beta H$ asym str def[3]	1030,1068
Ring breathing[3]	991
$C_\alpha H$, $C_\beta H$ asym wagg[3]	979
C-H str[4]	3058
C-C, C-N str[4]	1595, 1479, 1436
C-C in-plane bend[4]	1211
C-H in-plane bend[4]	1064
Asym ring breathing[4]	1035
Sym ring breathing[4]	1004
CH bend[4]	751
CH in-phase bend[4]	711

Table 4.6. Assignment of IR stretching frequencies for copper nanoparticles. Where sym str=symmetrical, asym=asymmetrical, str=stretch, v=vibration, def=deformation wagg=wagg. Numbers 1 to 4 denote assignment of the bands, 1 being assigned to oleylamine,[38,39] *2 for diphenyl ether,*[40,41] *3 for free pyridine,*[42] *4 for bound pyridine.*[43] †† assignments made from the literature values displayed in Table 4.5.

Assignment††	**Frequency / cm^{-1}**
=C-H v-bend[1]	3000, 2993
CH v-asym[1],	2926
CH v-sym[1]	2886
	1525
CH_3 v-bend[1], C-C, C-N str[4]	1486
	1381
O-C-O sym str[2], C-C in-plane bend[4]	1232
$C_\beta HC_\gamma H$ def[3]	1163
C-H in-plane bend[4], C-N v-bend[1], $C_\gamma H$ def, $C_\alpha H$, $C_\beta H$ sym str def[3]	1073
Asym ring breathing[4], $C_\alpha H$, $C_\beta H$ asym str def[3]	1022
	907
	865
CH oop bend[4]	748
C-C v-bend[1]	738
CH in-phase oop bend[4]	689
	636
	491

4.2. Results and discussion - bimetallic copper/silver nanoparticles

4.2.1. Silver nanoparticles from optimised copper nanoparticle conditions

The optimised copper conditions, which gave small monodisperse copper nanoparticles, were used for the synthesis of silver nanoparticles. The conditions used were 0.46 mmol of morpholine borane complex, with octadecylamine capping agent, with otherwise standard preparation conditions, as reported in Section 4.1.2.1.2 If these conditions gave silver nanoparticles with a suitably small particle size, and low dispersity then it was anticipated favourable results should be obtained when starting from two different metal salts as the conditions would not favour different products with the different metals.

As can be seen below in Figure 4.29, suitably small and monodisperse silver nanoparticles were synthesised using the same conditions as optimised for copper.

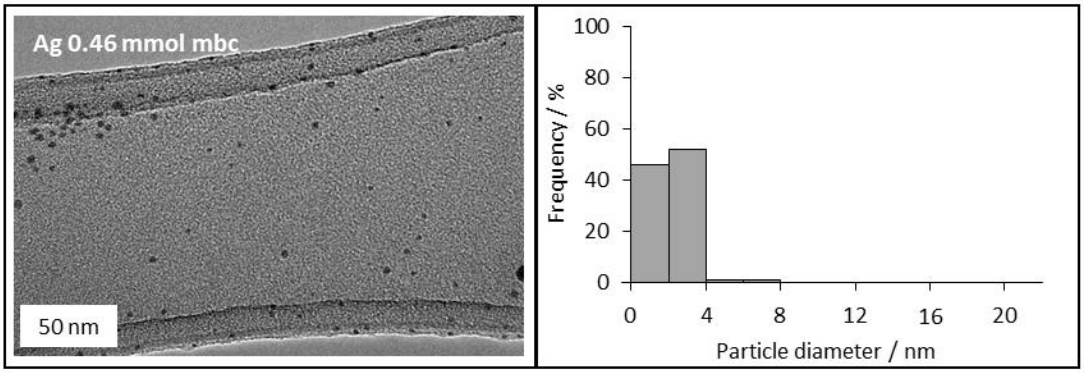

Figure 4.29. TEM images, and histograms calculated from measurement of particle diameter from TEM images for a minimum of 100 particles. With a particle size distribution of 2 ± 1 nm. For silver (Ag) nanoparticles synthesised according to Section 2.2.1.5.3 with 0.46 mmol morpholine borane complex (mbc), and octadecylamine capping agent Ag_290716_1 (see Section 2.2.1.6.1).

4.2.2. Bimetallic copper/silver nanoparticles

Bimetallic nanoparticles were synthesised, from this optimised preparation. Both metal precursors were added simultaneously, with the aim of giving nucleation of the silver and copper at the same time. However, the TEM images from this synthesis, given in Figure 4.30, show a wide variety of particle sizes with a wide size distribution. Note: the particle size distribution was in this case prepared from only two areas of the grid.

In order to attempt removal of the very large particles, the bimetallic synthesis was repeated. From Section 4.1.2.1.2, it was seen that for copper nanoparticle synthesis, an increase in the morpholine borane complex, from 0.46 mmol to 0.92 mmol with octadecylamine capping agent, gave a smaller average particle size and size dispersion. The bimetallic synthesis was repeated with the increased concentration of reducing agent, with the aim of creating small bimetallic nanoparticles only. However, no particles were seen by TEM for the resulting bimetallic preparation. The bimetallic nanoparticle solution was pink in colour, which might indicate a very large particle size.[44–47] It was believed that large agglomerates may have been formed and precipitated out of the solution.

In order to attempt reduction in the size of the resulting bimetallic, a smaller amount of reducing agent was used (Section 4.1.2). The resulting bimetallic was synthesised using 0.23 mmol of morpholine borane complex. It should be noted that a preparation temperature of 220 °C was used and an octadecylamine capping agent as both were not expected to have a large effect. These variables were chosen as a satisfactory result for this project's purpose was obtained before exploring all the possible variations of temperature and capping agent anticipated this was not continued. TEM imaging and particle size data are given in Figure 4.31. Small bimetallic particles, with a relatively low level of polydispersity were seen

(although still with some larger particles present). With higher magnification imaging showing the spherical appearance of the particle. Energy Dispersive X-ray (EDX) spectra were also obtained for this sample (Figure 4.32), showing both copper and silver were detected. Carbon and nickel signals originate predominantly from the TEM grids. Silicon was attributed to traces of silicone grease used to give a vacuum seal in the reaction to allow for an inert reaction atmosphere to be used (note it is likely this is incorporated during work up of the reactions as it can be difficult to remove the sample while completely excluding traces of silicone grease and it becomes concentrated when evaporated on the TEM grid).

Further optimisation in tuning particle size, or further reducing the size dispersity seen could be undertaken in further work, but at least as a proof of principle a sample with a reasonable small size distribution has been obtained (they are invariably larger for bimetallic nanoparticles).

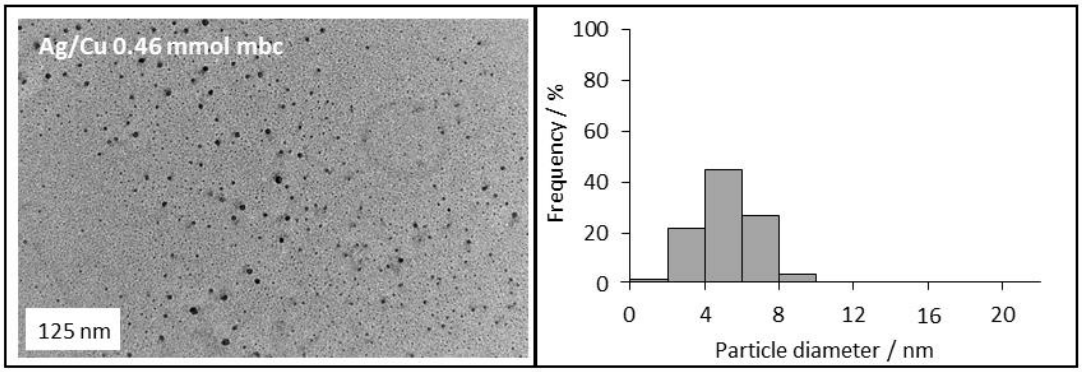

Figure 4.30. TEM images, and histograms calculated from measurement of particle diameter from TEM images for a minimum of 100 particles measured across 2 grid regions only. With a particle size distribution of 5 ± 2 nm. For silver and copper bimetallic nanoparticles (Ag/Cu), synthesised according to Section 2.2.1.6 with 0.46 mmol morpholine borane complex (mbc), and octadecylamine capping agent AgCu_010816_1 (Section 2.2.1.6.1).

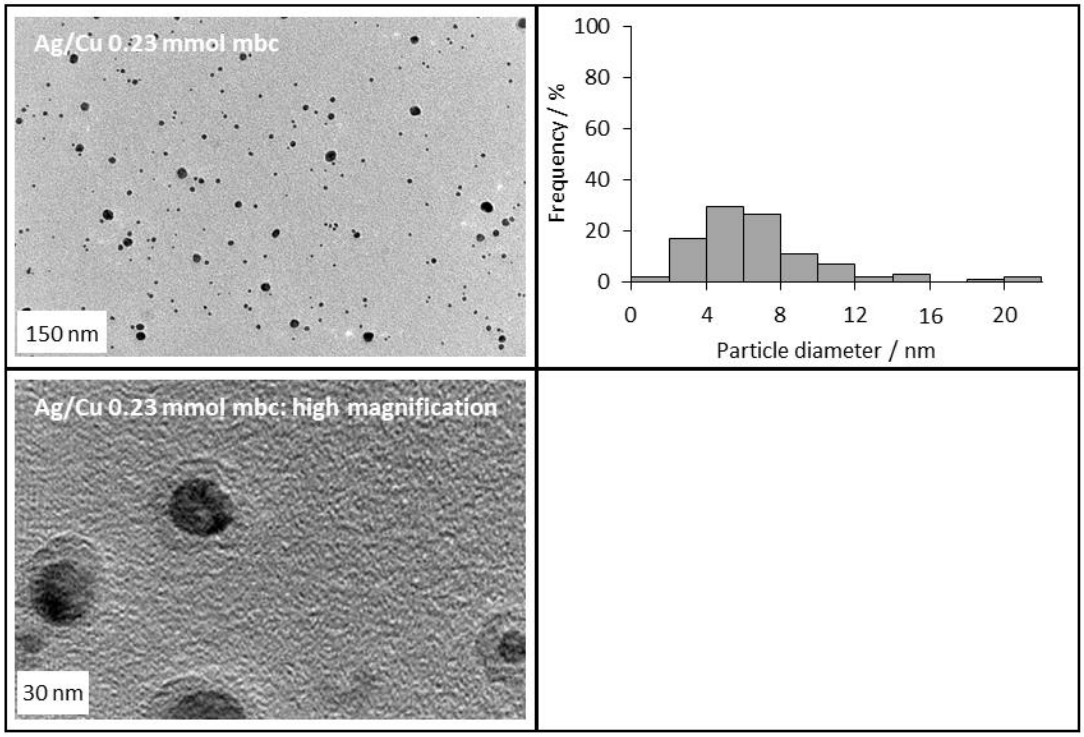

Figure 4.31. TEM images, and histograms calculated from measurement of particle diameter from TEM images for a minimum of 100 particles. With a particle size distribution of 7 ± 4 nm. For silver and copper bimetallic nanoparticles (Ag/Cu) synthesised according to Section 2.2.1.6 at 220 °C with 0.23 mmol morpholine borane complex (mbc), and octadecylamine capping agent AgCu_150816_1 (see Section 2.2.1.6.1). With higher magnification image shown below main image.

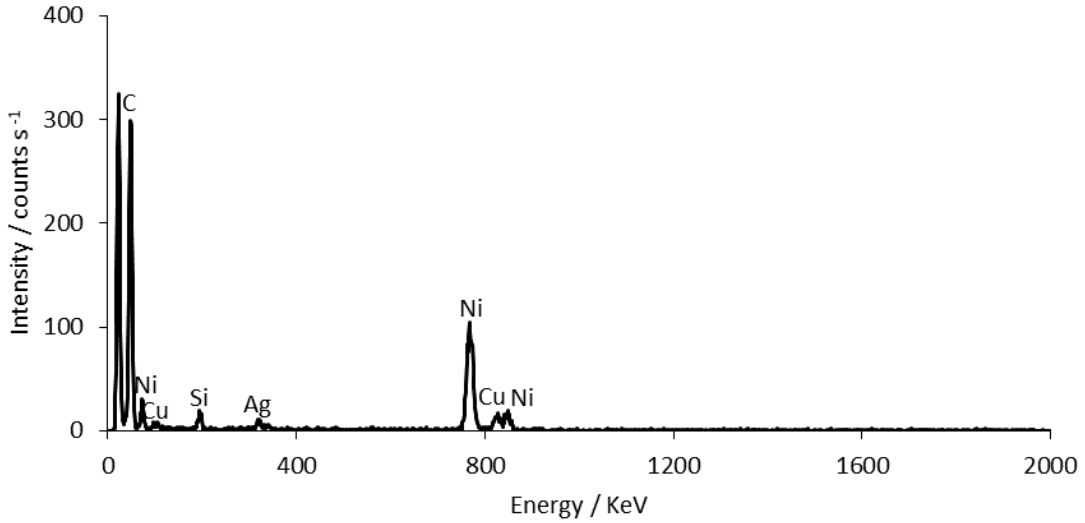

Figure 4.32. EDX spectra for silver and copper bimetallic nanoparticles on a carbon and nickel TEM grid. Nanoparticles were synthesised according to Section 2.2.1.6 with 0.23 mmol morpholine borane complex, and octadecylamine capping agent.

4.2.3. Further characterisation

4.2.3.1. Ultraviolet-visible (UV-vis) spectroscopy

Strong localised surface Plasmon resonances (LSPR) are seen for copper nanoparticles and can be observed using UV-vis spectroscopy. They are typically seen in the region 560-570 nm for larger copper nanoparticles.[48,49] For oligomeric clusters or super-small copper nanoparticles, typically with sizes below 5 nm, no LSPR is seen. Instead these species tend to show absorbance at much lower wavelengths typically in the region of 310 nm.[44,45,50] The presence of an oxidised copper surface, typically a copper oxide shell, causes weakening of the LSPR and a red shift is often seen. The extent of the weakening and red shift increases for higher levels of surface oxidation. Absorbances for oxidised copper surfaces are seen up to around 630 nm.[51]

For silver nanoparticles LSPR are typically seen around 420 nm,[52–55] and also vary with chemical environment, such as the presence of electron donating and withdrawing groups. Particle size is also seen to influence the LSPR wavelength. Depending upon the conditions both red and blue shifts can be seen.[54,56]

UV-vis spectroscopy is widely used in the literature as an indicator of nanoparticle size and structure. For completeness and future reference key samples were investigated here using UV-vis spectroscopy to identify whether LSPR signals were seen, and in conjunction with TEM imaging infer chemical environment, oxidation state, and particle size.

For copper nanoparticles with a TEM average particle diameter of 4.5 ± 0.8 nm the UV-vis spectra is given in Figure 4.33. No LSPR was seen and the maximum absorbance was centred around 290 nm, with two shoulders at 330 and 450 nm. One of the three bands (330 nm) might be assigned to ultra-small copper nanoparticles as per references above, and the absence of the LSPR band was expected for the small sized nanoparticles. Analysis of High Resolution Electron Microscopy (HREM) TEM images reveal lighter regions, around the very edge of the nanoparticle, attributed to the presence of a copper oxide shell. An example of this is given in Figure 4.37 for cobalt nanoparticles with a visible oxide shell. Hence another of the shoulders bands could be attributed to the copper oxide shell – if red shifted this could be the feature at 450 nm. To identify the other band at 290 nm, it was realised that the organic capping agent present at the surface of the nanoparticles could also contribute and so UV-vis spectra of oleylamine was obtained (Figure 4.34). The spectrum obtained was for a sample containing 0.018 mL of oleylamine per 1 mL of hexane, so as to correspond to the concentration used in reaction and therefore the maximum amount of capping agent present

on the nanoparticle surface. The spectrum shows a strong absorbance centred around 297 nm. Overall this allows the three bands seen for the copper nanoparticles to be assigned as oleylamine at 290 nm, ultra-small copper nanoparticles at 330 nm, and copper oxide shell at 450 nm, in line with the typical literature values discussed above.

For silver nanoparticles the UV-vis spectra was given in Figure 4.35. Two absorbances were seen. The weakest at 290 nm can be attributed to the oleylamine capping agent as before. The second stronger band at 410 nm can be attributed to the LSPR for silver. The silver nanoparticles had an average particle diameter of 4.1 ± 0.8 nm. The wavelength of the LSPR is fairly typical for silver nanoparticles, though may be a little blue shifted due to the small size of the particles.

Finally for bimetallic nanoparticles of average particle diameter 5.1 ± 3.2 nm the UV-vis spectrum, given in Figure 4.36, showed one strong absorbance around 400 nm, which is very broad, with a second band around 290 nm of significant intensity. The 290 nm feature can again be ascribed to oleylamine. The main band is likely to be due to the LPSR of silver or silver copper. Core-shell type structures are common for bimetallics.[57–62] A copper core and silver shell type structure would be expected to give a similar spectrum to that seen for pure silver. The significant broadening could speculatively be suggested to arise from either multiple sizes (due to greater polydispersity) or surface silver-copper compositions, but indicated a change that is different from a simple sum of the pure silver and pure copper particles.

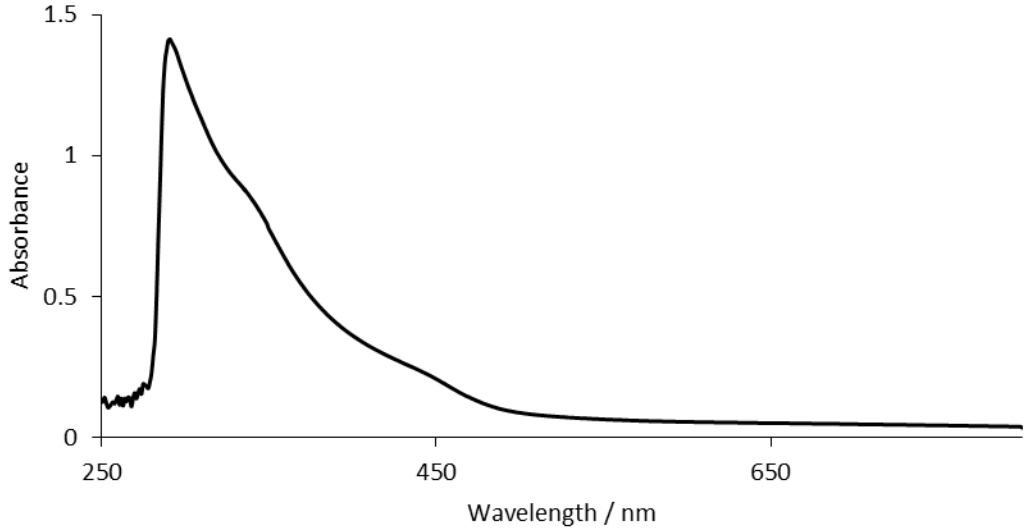

Figure 4.33. UV-vis spectra taken for copper nanoparticles in hexane reference solvent. For copper nanoparticles synthesised at 200 °C with a 1 h ripening time with an oleylamine capping agent (2.2 mmol, where 1.1 mmol is used in typical preparations as described in Section 2.2.1.5), and in the absence of reducing agent with sample reference Cu-010316_1 (see Appendix, particle size 34 ± 5 nm).

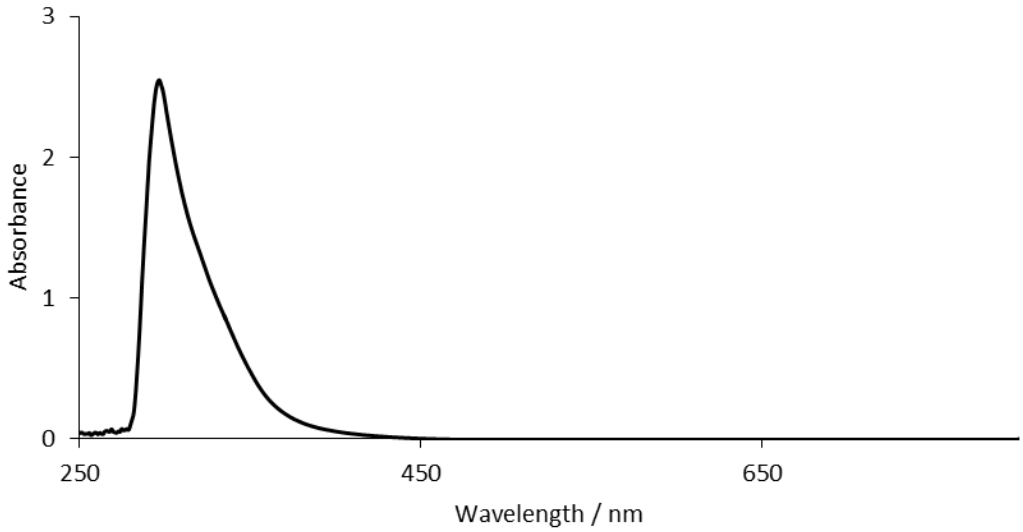

Figure 4.34. UV-vis spectra taken for oleylamine in hexane reference solvent.

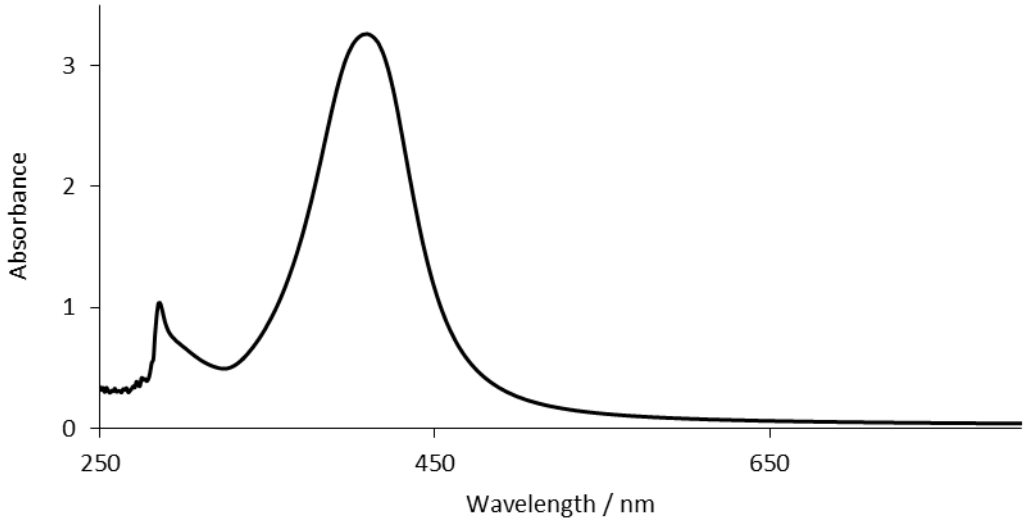

Figure 4.35. UV-vis spectra taken for silver nanoparticles in hexane reference solvent. For silver nanoparticles synthesised at 200 °C, with a 1 h ripening time, with an oleylamine capping agent, and with stoichiometric addition of morpholine borane complex, (0.23 mmol morpholine borane complex:0.23 mmol silver(I) acetylacetonate (as described in Section 2.2.1.5.3) with sample reference Ag-090316_1 (see Section 2.2.1.6.1, particle size 6 ± 2 nm).

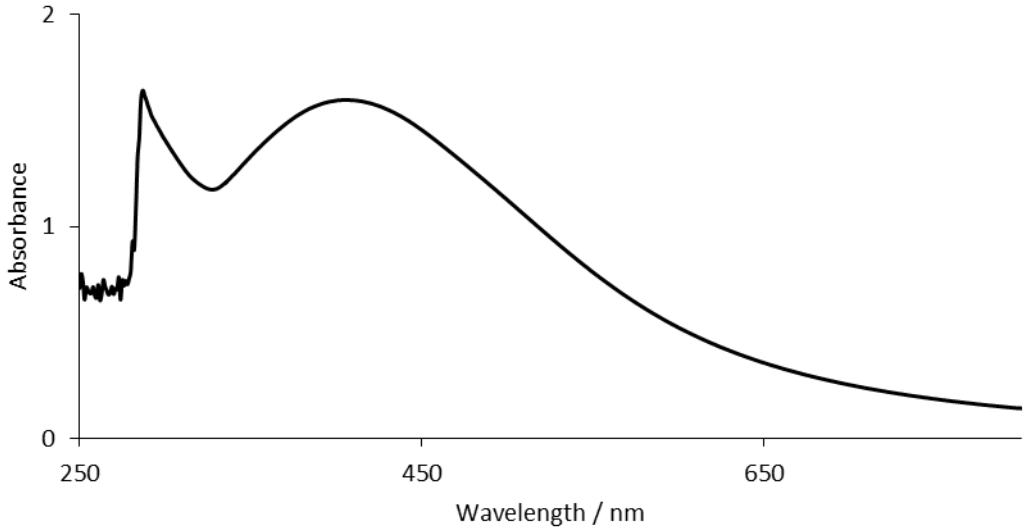

Figure 4.36. UV-vis spectra taken for silver/copper bimetallic nanoparticles in hexane reference solvent. For nanoparticles synthesised at 200 °C, with a 1 h ripening time, with an oleylamine capping agent, and with stoichiometric addition of morpholine borane complex, (0.23 mmol morpholine borane complex:0.23 mmol copper(II) acetylacetonate) (as described in Section 2.2.1.6) with sample reference AgCu-150316_1 (see Section 2.2.1.6.1, particle size 5 ± 3 nm).

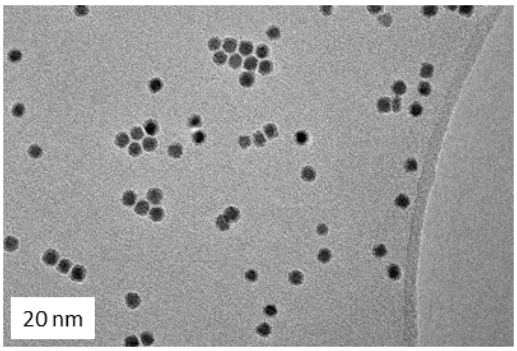

Figure 4.37. TEM imaging for cobalt nanoparticles with a light outer region attributed to an oxide shell. [63]

4.2.3.2. ICP-OES analysis

ICP-OES analysis was conducted for both monometallic copper, and bimetallic nanoparticles. Typical values obtained are given in Table 4.7 below (A more complete list of ICP-OES results can be found in the Appendix). A range of nanoparticle synthesis yields based on the expected copper content were found, but all values were above 50%. This indicates acceptable conversions for typical nanoparticle preparations and confirms extensive decomposition due to metal ion oxidation has not occurred.[64]

For the bimetallic nanoparticles (Table 4.7 sample D) the copper yield was similar to that seen for pure copper synthesised under identical conditions (Table 4.7 sample A). The silver recovery was higher than for the copper (perhaps as less easily re-oxidised once reduced), and the values indicated a good level of conversion of the metal salt to the metal nanoparticle. Any unconverted material or decomposed oxidised ions were removed by vigorous washing prior to ICP-OES analysis.

Table 4.7. Typical ICP-OES conversion values for monometallic copper (Cu) nanoparticles and bimetallic (Ag and Cu) nanoparticles, digested in nitric acid and aqua regia respectively. All samples were washed thoroughly prior to ICP-OES analysis (see Section 2.2.1.5 and 2.2.1.6 for details) to remove any un-reacted metal salt, or decomposed oxidised metal ions. Nanoparticles were synthesised, with the following parameters varied and sample identifiers A) octadecylamine capping agent used Cu-170616_1, B) 0.92 mmol morpholine borane complex used Cu-130716_1, C) 0.23 mmol morpholine borane complex used Cu-040516_1, D) octadecylamine capping agent AgCu-150816_1 (see Appendix, and Section 2.2.1.6.1).

Sample	Yield Cu / %	Yield Ag / %
A	66	N/A
B	76	N/A
C	85	N/A
D	62	93

4.2.4. Chapter 4 conclusions

Key conclusions from the variation of a number of parameters, and observations about their impact upon pure copper nanoparticle formation are as follows:

- In the absence of reducing agent large particles are formed, which appear from TEM imaging to initially comprise of multiple smaller particles that have coalesced. At longer times and higher temperatures these become more strongly faceted, likely so that low energy surface facets dominate.
- Morpholine borane complex functions as an effective reducing agent, likely *via* a burst nucleation process, when used in >1:1 ratio with the copper(II) acetylacetonate metal precursor, resulting in small particles with tight size distributions, with both octadecylamine and oleylamine capping agents.
- An alkane-diol reducing agent similar to that reported in the literature did not show evidence of leading to efficient reduction *via* burst nucleation, and instead led to large faceted particles several hundred nanometres in size.
- Octadecylamine capping agent allows for formation of the smallest particles with the tightest size distribution.
- 1 h ripening period allowed an equilibrium distribution to be reached, even in the absence of reducing agent, as few further changes were seen after this time.

Optimised synthesis conditions using octadecylamine, >1:1 Morpholine borane complex:copper(II) acetylacetonate molar ratio at 200 °C was therefore used as the starting point for attempted synthesis of bimetallic nanoparticles. Bimetallic silver/copper nanoparticles have been synthesised in a targeted approach based on their monometallic counterparts, and small bimetallic particles with a reasonably low size dispersity were obtained. Further optimisation of this preparation could be conducted, including the use of sequential addition of the two metal salts. This would give staggered silver and copper nanoparticle nucleation, and could have a significant impact upon the properties of the particles obtained.

UV-vis spectroscopy was obtained for key samples and interpreted based upon the literature, so as to allow future comparisons to the work carried out here using a widely accessible and straightforward technique.

ICP-OES was used to obtain yields (based on copper or silver content) for nanoparticles synthesised, and key results were discussed. Yields consistently >50% demonstrate the

synthesis routes established can be used to generate reasonable quantities of the intended product.

4.3. Bibliography

(1) Salavati-Niasari, M.; Davar, F. Synthesis of Copper and Copper (I) Oxide Nanoparticles by Thermal Decomposition of a New Precursor. *Mater. Lett.* **2009**, *63* (3), 441–443.

(2) Benkovičová, M.; Végsö, K.; Šiffalovič, P.; Jergel, M.; Majková, E.; Luby, Š.; Šatka, A. Preparation of Sterically Stabilized Gold Nanoparticles for Plasmonic Applications. *Chem. Pap.* **2013**, *67* (9).

(3) Xu, Z.; Shen, C.; Hou, Y.; Gao, H.; Sun, S. Oleylamine as Both Reducing Agent and Stabilizer in a Facile Synthesis of Magnetite Nanoparticles. *Chem. Mater.* **2009**, *21* (9), 1778–1780.

(4) Chen, M.; Feng, Y. G.; Wang, X.; Li, T. C.; Zhang, J. Y.; Qian, D. J. Silver Nanoparticles Capped by Oleylamine: Formation, Growth, and Self-Organization. *Langmuir* **2007**, *23* (10), 5296–5304.

(5) Mourdikoudis, S.; Liz-Marzán, L. M. Oleylamine in Nanoparticle Synthesis. *Chem. Mater.* **2013**, *25* (9), 1465–1476.

(6) Yu, Y.; Yang, W.; Sun, X.; Zhu, W.; Li, X. Z.; Sellmyer, D. J.; Sun, S. Monodisperse MPt (M = Fe, Co, Ni, Cu, Zn) Nanoparticles Prepared from a Facile Oleylamine Reduction of Metal Salts. *Nano Lett.* **2014**, *14* (5), 2778–2782.

(7) Mott, D.; Galkowski, J.; Wang, L.; Luo, J.; Zhong, C. J. Synthesis of Size-Controlled and Shaped Copper Nanoparticles. *Langmuir* **2007**, *23* (10), 5740–5745.

(8) Hoene, J. V.; Charles, R. G.; Hickam, W. M. Thermal Decomposition of Metal Acetylacetonates: Mass Spectrometer Studies. *J. Phys. Chem.* **1958**, *62* (9), 1098–1101.

(9) Pileni, M. P.; Ninham, B. W.; Gulik-Krzywicki, T.; Tanori, J.; Lisiecki, I.; Filankembo, A. Direct Relationship between Shape and Size of Template and Synthesis of Copper Metal Particles. *Adv. Mater.* **1999**, *11* (16), 1358–1362.

(10) Chen, S.; Sommers, J. M. Alkanethiolate-Protected Copper Nanoparticles: Spectroscopy, Electrochemistry, and Solid-State Morphological Evolution†. *J. Phys. Chem. B* **2001**, *105* (37), 8816–8820.

(11) Petroski, J. M.; Wang, Z. L.; Green, T. C.; El-Sayed, M. A. Kinetically Controlled Growth and Shape Formation Mechanism of Platinum Nanoparticles. *J. Phys. Chem. B* **1998**, *102* (18), 3316–3320.

(12) Peng, Z. A.; Peng, X. Mechanisms of the Shape Evolution of CdSe Nanocrystals. *J. Am. Chem. Soc.* **2001**, *123* (7), 1389–1395.

(13) Grzelczak, M.; Pérez-Juste, J.; Mulvaney, P.; Liz-Marzán, L. M. Shape Control in Gold Nanoparticle Synthesis. *Chem. Soc. Rev.* **2008**, *37* (9), 1783.

(14) Barmparis, G. D.; Lodziana, Z.; Lopez, N.; Remediakis, I. N. Nanoparticle Shapes by Using Wulff Constructions and First-Principles Calculations. *Beilstein J. Nanotechnol.* **2015**, *6*, 361–368.

(15) Crouse, C. A.; Barron, A. R. Reagent Control over the Size, Uniformity, and Composition of Co–Fe–O Nanoparticles. *J. Mater. Chem.* **2008**, *18* (35), 4146.

(16) Koski, K. J.; Kamp, N. M.; Smith, R. K.; Kunz, M.; Knight, J. K.; Alivisatos, A. P. Structural Distortions in 5–10 Nm Silver Nanoparticles under High Pressure. *Phys. Rev. B* **August 10**, *78* (16), 165410.

(17) Yang, Y.; Chen, H.; Zhao, B.; Bao, X. Size Control of ZnO Nanoparticles via Thermal Decomposition of Zinc Acetate Coated on Organic Additives. *J. Cryst. Growth* **2004**, *263* (1), 447–453.

(18) Navaladian, S.; Viswanathan, B.; Viswanath, R. P.; Varadarajan, T. K. Thermal Decomposition as Route for Silver Nanoparticles. *Nanoscale Res. Lett.* **2007**, *2* (1), 44–48.

(19) Lidor-Shalev, O.; Zitoun, D. Reaction Mechanism of “amine–borane Route” towards Sn, Ni, Pd, Pt Nanoparticles. *RSC Adv* **2014**, *4* (109), 63603–63610.

(20) Zheng, N.; Fan, J.; Stucky, G. D. One-Step One-Phase Synthesis of Monodisperse Noble-Metallic Nanoparticles and Their Colloidal Crystals. *J. Am. Chem. Soc.* **2006**, *128* (20), 6550–6551.

(21) Peng, S.; Lee, Y.; Wang, C.; Yin, H.; Dai, S.; Sun, S. A Facile Synthesis of Monodisperse Au Nanoparticles and Their Catalysis of CO Oxidation. *Nano Res.* **2008**, *1* (3), 229–234.

(22) Mazumder, V.; Sun, S. Oleylamine-Mediated Synthesis of Pd Nanoparticles for Catalytic Formic Acid Oxidation. *J. Am. Chem. Soc.* **2009**, *131* (13), 4588–4589.

(23) Kalidindi, S. B.; Sanyal, U.; Jagirdar, B. R. Metal Nanoparticles via the Atom-Economy Green Approach. *Inorg. Chem.* **2010**, *49* (9), 3965–3967.

(24) Baitalow, F.; Baumann, J.; Wolf, G.; Jaenicke-Rößler, K.; Leitner, G. Thermal Decomposition of B–N–H Compounds Investigated by Using Combined Thermoanalytical Methods. *Thermochim. Acta* **2002**, *391* (1), 159–168.

(25) Wolf, G.; Baumann, J.; Baitalow, F.; Hoffmann, F. . Calorimetric Process Monitoring of Thermal Decomposition of B–N–H Compounds. *Thermochim. Acta* **2000**, *343* (1–2), 19–25.

(26) Stephens, F. H.; Pons, V.; Tom Baker, R. Ammonia–borane: The Hydrogen Source Par Excellence? *Dalton Trans* **2007**, No. 25, 2613–2626.

(27) Denney, M. C.; Pons, V.; Hebden, T. J.; Heinekey, D. M.; Goldberg, K. I. Efficient Catalysis of Ammonia Borane Dehydrogenation. *J. Am. Chem. Soc.* **2006**, *128* (37), 12048–12049.

(28) Keaton, R. J.; Blacquiere, J. M.; Baker, R. T. Base Metal Catalyzed Dehydrogenation of Ammonia−Borane for Chemical Hydrogen Storage. *J. Am. Chem. Soc.* **2007**, *129* (7), 1844–1845.

(29) Stowe, A. C.; Shaw, W. J.; Linehan, J. C.; Schmid, B.; Autrey, T. In Situ Solid State 11B MAS-NMR Studies of the Thermal Decomposition of Ammonia Borane: Mechanistic Studies of the Hydrogen Release Pathways from a Solid State Hydrogen Storage Material. *Phys. Chem. Chem. Phys.* **2007**, *9* (15), 1831.

(30) Kalidindi, S. B.; Joseph, J.; Jagirdar, B. R. Cu2+-Induced Room Temperature Hydrogen Release from Ammonia Borane. *Energy Environ. Sci.* **2009**, *2* (12), 1274.

(31) Cheng, F.; Ma, H.; Li, Y.; Chen, J. $Ni_{1-x}Pt_x$ (X = 0−0.12) Hollow Spheres as Catalysts for Hydrogen Generation from Ammonia Borane. *Inorg. Chem.* **2007**, *46* (3), 788–794.

(32) Clark, T. J.; Whittell, G. R.; Manners, I. Highly Efficient Colloidal Cobalt- and Rhodium-Catalyzed Hydrolysis of $H_3N{\cdot}BH_3$ in Air. *Inorg. Chem.* **2007**, *46* (18), 7522–7527.

(33) Chandra, M.; Xu, Q. Room Temperature Hydrogen Generation from Aqueous Ammonia-Borane Using Noble Metal Nano-Clusters as Highly Active Catalysts. *J. Power Sources* **2007**, *168* (1), 135–142.

(34) Kalidindi, S. B.; Sanyal, U.; Jagirdar, B. R. Nanostructured Cu and $Cu@Cu_2O$ Core Shell Catalysts for Hydrogen Generation from Ammonia–borane. *Phys. Chem. Chem. Phys.* **2008**, *10* (38), 5870.

(35) Brown, H. C.; Murray, L. T. Molecular Addition Compounds. 9. Effect of Structure on the Reactivities of Representative Borane-Amine Complexes in Typical Reactions such as Hydrolysis, Hydroboration, and Reduction. *Inorg. Chem.* **1984**, *23* (18), 2746–2753.

(36) Ramachandran, P. V.; Kulkarni, A. S.; Pfeil, M. A.; Dennis, J. D.; Willits, J. D.; Heister, S. D.; Son, S. F.; Pourpoint, T. L. Amine-Boranes: Green Hypergolic Fuels with Consistently Low Ignition Delays. *Chem. Eur. J.* **2014**, *20* (51), 16869–16872.

(37) Jana, N. R.; Gearheart, L.; Murphy, C. J. Seeding Growth for Size Control of 5−40 Nm Diameter Gold Nanoparticles. *Langmuir* **2001**, *17* (22), 6782–6786.

(38) Shukla, N.; Liu, C.; Jones, P. M.; Weller, D. FTIR Study of Surfactant Bonding to FePt Nanoparticles. *J. Magn. Magn. Mater.* **2003**, *266* (1–2), 178–184.

(39) Zhang, J. L.; Srivastava, R. S.; Misra, R. D. K. Core−Shell Magnetite Nanoparticles Surface Encapsulated with Smart Stimuli-Responsive Polymer: Synthesis, Characterization, and LCST of Viable Drug-Targeting Delivery System. *Langmuir* **2007**, *23* (11), 6342–6351.

(40) Oxley, J.; Smith, J.; Brady, J.; Dubnikova, F.; Kosloff, R.; Zeiri, L.; Zeiri, Y. Raman and Infrared Fingerprint Spectroscopy of Peroxide-Based Explosives. *Appl. Spectrosc.* **2008**, *62* (8), 906–915.

(41) Naidu, A. B.; Jaseer, E. A.; Sekar, G. General, Mild, and Intermolecular Ullmann-Type Synthesis of Diaryl and Alkyl Aryl Ethers Catalyzed by Diol−Copper(I) Complex †. *J. Org. Chem.* **2009**, *74* (10), 3675–3679.

(42) Visak, Z. P.; Ilharco, L. M.; Garcia, A. R.; Najdanovic-Visak, V.; Fareleira, J. M. N. A.; Caetano, F. J. P.; Kijevcanin, M. L.; Serbanovic, S. P. Volumetric Properties and Spectroscopic Studies of Pyridine or Nicotine Solutions in Liquid Polyethylene Glycols. *J. Phys. Chem. B* **2011**, *115* (26), 8481–8492.

(43) Haq, S.; King, D. A. Configurational Transitions of Benzene and Pyridine Adsorbed on Pt{111} and Cu{110} Surfaces: An Infrared Study. *J. Phys. Chem.* **1996**, *100* (42), 16957–16965.

(44) Athawale, A. A.; Katre, P. P.; Kumar, M.; Majumdar, M. B. Synthesis of CTAB–IPA Reduced Copper Nanoparticles. *Mater. Chem. Phys.* **2005**, *91* (2–3), 507–512.

(45) Khatouri, J.; Mostafavi, M.; Amblard, J.; Belloni, J. Radiation-Induced Copper Aggregates and Oligomers. *Chem. Phys. Lett.* **1992**, *191* (3–4), 351–356.

(46) Kapoor, S. Preparation, Characterization, and Surface Modification of Silver Particles. *Langmuir* **1998**, *14* (5), 1021–1025.

(47) Kapoor, S.; Joshi, R.; Mukherjee, T. Influence of I−Anions on the Formation and Stabilization of Copper Nanoparticles. *Chem. Phys. Lett.* **2002**, *354* (5–6), 443–448.

(48) Wu, S. H.; Chen, D. H. Synthesis of High-Concentration Cu Nanoparticles in Aqueous CTAB Solutions. *J. Colloid Interface Sci.* **2004**, *273* (1), 165–169.

(49) Dang, T. M. D.; Le, T. T. T.; Fribourg-Blanc, E.; Dang, M. C. Synthesis and Optical Properties of Copper Nanoparticles Prepared by a Chemical Reduction Method. *Adv. Nat. Sci. Nanosci. Nanotechnol.* **2011**, *2* (1), 015009.

(50) Siwach, O. P.; Sen, P. Synthesis and Study of Fluorescence Properties of Cu Nanoparticles. *J. Nanoparticle Res.* **2008**, *10* (S1), 107–114.

(51) Kanninen, P.; Johans, C.; Merta, J.; Kontturi, K. Influence of Ligand Structure on the Stability and Oxidation of Copper Nanoparticles. *J. Colloid Interface Sci.* **2008**, *318* (1), 88–95.

(52) Filippo, E.; Serra, A.; Manno, D. Poly(vinyl Alcohol) Capped Silver Nanoparticles as Localized Surface Plasmon Resonance-Based Hydrogen Peroxide Sensor. *Sens. Actuators B Chem.* **2009**, *138* (2), 625–630.

(53) Lawandy, N. M. Localized Surface Plasmon Singularities in Amplifying Media. *Appl. Phys. Lett.* **2004**, *85* (21), 5040.

(54) Pal, S.; Tak, Y. K.; Song, J. M. Does the Antibacterial Activity of Silver Nanoparticles Depend on the Shape of the Nanoparticle? A Study of the Gram-Negative Bacterium Escherichia Coli. *Appl. Environ. Microbiol.* **2007**, *73* (6), 1712–1720.

(55) Vigneshwaran, N.; Ashtaputre, N. M.; Varadarajan, P. V.; Nachane, R. P.; Paralikar, K. M.; Balasubramanya, R. H. Biological Synthesis of Silver Nanoparticles Using the Fungus Aspergillus Flavus. *Mater. Lett.* **2007**, *61* (6), 1413–1418.

(56) Mogensen, K. B.; Kneipp, K. Size-Dependent Shifts of Plasmon Resonance in Silver Nanoparticle Films Using Controlled Dissolution: Monitoring the Onset of Surface Screening Effects. *J. Phys. Chem. C* **2014**, *118* (48), 28075–28083.

(57) Grouchko, M.; Kamyshny, A.; Magdassi, S. Formation of Air-Stable Copper–silver Core–shell Nanoparticles for Inkjet Printing. *J. Mater. Chem.* **2009**, *19* (19), 3057.

(58) Lu, L.; Wang, H.; Zhou, Y.; Xi, S.; Zhang, H.; Hu, J.; Zhao, B. Seed-Mediated Growth of Large, Monodisperse Core–shell Gold–silver Nanoparticles with Ag-like Optical Properties. *Chem. Commun.* **2002**, No. 2, 144–145.

(59) Shankar, S. S.; Rai, A.; Ahmad, A.; Sastry, M. Rapid Synthesis of Au, Ag, and Bimetallic Au core–Ag Shell Nanoparticles Using Neem (Azadirachta Indica) Leaf Broth. *J. Colloid Interface Sci.* **2004**, *275* (2), 496–502.

(60) Baletto, F.; Mottet, C.; Ferrando, R. Growth Simulations of Silver Shells on Copper and Palladium Nanoclusters. *Phys. Rev. B* **2002**, *66* (15).

(61) Zhong, C. J.; Maye, M. M. Core–Shell Assembled Nanoparticles as Catalysts. *Adv. Mater.* **2001**, *13* (19), 1507–1511.

(62) Srnová-Šloufová, I.; Lednický, F.; Gemperle, A.; Gemperlová, J. Core−Shell (Ag)Au Bimetallic Nanoparticles: Analysis of Transmission Electron Microscopy Images. *Langmuir* **2000**, *16* (25), 9928–9935.

(63) Saison, C.; Perreault, F.; Daigle, J. C.; Fortin, C.; Claverie, J.; Morin, M.; Popovic, R. Effect of Core–shell Copper Oxide Nanoparticles on Cell Culture Morphology and Photosynthesis (Photosystem II Energy Distribution) in the Green Alga, Chlamydomonas Reinhardtii. *Aquat. Toxicol.* **2010**, *96* (2), 109–114.

(64) Isarov, A. V.; Chrysochoos, J. Optical and Photochemical Properties of Nonstoichiometric Cadmium Sulfide Nanoparticles: Surface Modification with Copper(II) Ions. *Langmuir* **1997**, *13* (12), 3142–3149.